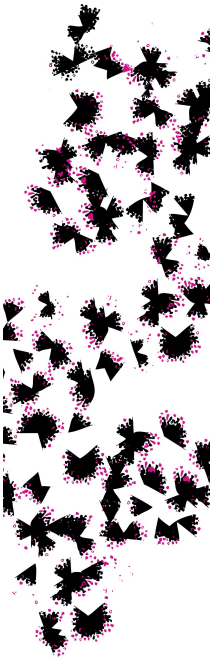

Development of PI-ETPU based sensors for prosthesis control

P.R. (Pedro) Dias

MSc Report

Committee:
Prof.dr.ir. G.J.M. Krijnen
G.J. Wolterink, MSc
Dr.M. Satori
Ing. R.G.P. Sanders

August 2018

034RAM2018
Robotics and Mechatronics
EE-Math-CS
University of Twente
P.O. Box 217
7500 AE Enschede
The Netherlands

Acknowledgements

- M. Isabel Silva, Humberto Dias, Cidália Silva, Diamantino Silva, Rute Silva.
- Ana Carolina Oliveira, Beatriz Gonçalves, Diogo Abreu, Inês Prior, João Francisco Luís, Joana Ramos, M. Margarida Mendonça, Nuno Nora, Rita Alvelos, Sara Martins.
- Antonio Gogeascoechea, Carolina Correia, João Pedro Baptista, Maria Enes, Mariana Hugo, Ricardo Margarido.
- Gijs Krijnen, Gerjan Wolterink, Massimo Sartori, Remco Sanders

Contents

Chapter 1

Introduction

1.1 Context

In 2018 there is still a huge gap in the market of prosthesis. On one side of the spectrum there are very simple, inexpensive products that have little applicability in day-to-day activities. On the other side of the spectrum there are devices with an extremely high level of complexity that are able to give subjects a great quality of life but that never reach the market mainly due to cost limitations.

The project that is going to be presented in this report was developed at the RAM department of the University of Twente as part of the SoftPro project. This project aims for the development of novel techniques in robotics to develop new prosthesis, amongst other types of devices, particularly focusing on upper limb rehabilitation. In this report it will be shown that there are several problems hindering the development of upper limb prosthesis, one in particular being the price of electrodes. Electrodes are an essential component of rehabilitation as they allow for the gathering of myoelectric (EMG) signals. These only provide information regarding the muscles itself but they can also be used in order to control the prosthesis.

Looking at this particular problem and at the currently available technologies, we set out to find solutions to this problem in particular. For clinical applications there are sets of electrodes that are considered the gold standard of the industry, there are silver chloride (AgCl) electrodes, which have a very low impedance and allow for EMG signals to be recorded to good accuracy and little amounts of noise. Despite these facts these electrodes have limitations that hinder their application on a continuous and day-to-day application.

Recent developments in additive manufacturing (AM) and the wides pread of low-cost printers have boosted the market for all types of building filaments. Amongst them, there has been a rise of thermoplastic materials such as thermoplastic polyurethane (TPU) that still exists, but in a more interesting form for this project, which is in the form of electrically con-

ductive TPU filament, called Pi-ETPU. This material, as the name so says, is electrically conductive, and since it's a thermoplastic material produced for mainstream additive manufacturing, we are able to create any structures we deem fit with them.
Due to its relative low cost, and taking full advantage of 3D-printing technology, this report starts off by asking whether we can use these technologies in order to produce a change in the paradigm of the prosthetics industry. The goal of this project is to prove that a set of 3D-printed electrodes can be used in order to perform real-time gesture detection. In order to do this we are also going to look at the accuracy of the system and how it compares to silver chloride electrodes (AgCl), as these are considered the gold standard electrodes in the industry. Furthermore, before setting off on this ambitious journey, we are going to look at the material properties and how they can be used in order to find the ideal shape and size of the electrodes.

1.2 Project Goal

The following project is comprised of a series of goals. The first goal of this project would be to understand the effects of printing settings on the conductive properties of the conductive material in question. The second goal would be to develop one electrode with this material and perform its electrical characterisation (and see how it compares with the gold standard). Last but not least, in order to prove the real-life applicability of the new electrode, an armband comprised of this new electrode should have the approximate gesture classification capabilities as the one comprised of the gold standard electrodes.

1.3 Approach

The approach for achieving the goals set out in this report will be done by combining engineering and scientific approaches. First on an engineering level to perform tests that analyse structures and catalog their behaviour and later to find a plausible explanation for such behaviour.

1.4 Report Structure

The structure of the following report goes as follows, Chapter 2 will look at the state of the art of the several components that will be used in this project. For example, the latest developments in 3D printing and biomedical products achieved with this. How EMGs for real-time

prosthesis are being classified and what the latest advances in prosthetics are. Chapter 3 makes the first approach in the understading of how printing properties are affecting the electrical conductivity of a structure made of Pi-ETPU. The insight retrieved from this chapter lead to Chapter 4, where the first electrodes made of Pi-ETPU are being printed and their impedance measurements are being compared to the gold standard AgCl electrode. Following this, Chapter 5 will first present all the conceptual background in signal processing and machine-learning algorithms that is implemented to process the EMG signals provided by the electrodes and used to classify movement. Using this initial knowledge, the first comparison between an 8-electrode AgCl system and a 8-Electrode Pi-ETPU system is done. The results shown in this chapter evolve into Chapter 6 where the size and number of electrodes are varied in order to see how this affects the classification performance. Furthermore, in order to prove the wide applicability of the system, tests will be performed using two different subjects. In the last chapter a set of conclusions, future research and insights regarding industry applicability will be presented.

Chapter 2

State of the Art

2.1 Upper Limb Prosthesis

2.1.1 The Industry

The researched presented in this report focuses on the development of upper limb prostheses for the SoftPro Project. An upper limb prosthesis is a device that aims to replace the function of an upper limb for means of therapy, or to substitute it, in case of an amputation. Prostheses have been developed over the centuries, but only lately, with the surging of small technology, have these been truly fascinating to study. The simplest case of a prosthesis is a passive one, which aims to replace the body part and has very limited levels of functionality. Then there are mechanical (where the control of the prosthesis is done exclusively via the use of a joystick or hinges) and myoelectrically powered prostheses [1].
Companies such as OttoBlock, TouchBionics and Ossur have been making valuable progress in the control of upper limb prosthetics. For example, Figure 2.1 depicts the i-limb from Touch Bionics, which is one of their latest products. The subject is able to control the prosthesis via 4 different possibilities [2]: Gesture, App, Muscle, Proximity. A single case study regarding the i-limb ([3]) compares the i-limb with a DMC-plus (another prosthetic hand but from Otto-Block), and the results show that, because of the low familiarity in low training data, the score of the i-limb does not rank up. On the other hand, the results of the survey have shown that, due to the high training data, this was improving the system of the i-limb and the familiarity of the user with the device. That being said, the predicted cost for implementation of the i-limb system can vary from 60k to upwards of 120k USD([4]). The price of a prosthesis is not its only limitation; as it was presented, users do not autonomically adapt to the prosthesis and, not only that, they are still unable to mimic an arm in terms of grasp type, precision of finger dexterity and feedback of the prosthesis.

Figure 2.1: Hand Prosthesis from Touch Bionics

2.1.2 Myoelectric Control

As it was presented, there are several ways of controlling a prosthesis, one of them being via myoelectric control. Myoelectric control of a prosthesis looks into the electrical information of the muscles of the arm and looks to control a prosthesis with it. Electromyography (EMG) contains a lot of relevant information for the control of prostheses, such as the fact that different gestures and movements of the arm require different activations of muscles and muscle groups. Furthermore, the intensity and velocity of the movement is also related to the amplitude of the EMG signal.

Despite the big potential of these signals for the control of prostheses, practical systems are extremely complicated to build. More specifically, these systems, when compared to mechanical ones, where the movement of the arm and its connection to hinges and actuators leads to the movement of the prosthesis, a myoelectric system requires, on top of the actuators and other components that are included in a mechanical system, batteries, processors and electrodes to read signals, process and classify them, and produce an output [5]. All these requirements need to be fulfilled whilst not compromising the functionality of the prostheses, which means that it should remain light-weight, compact, and it should have high enough degrees of freedom in order to perform daily tasks. Several examples regarding this type of development are presented in [6], [7]. The concept of myoelectric control of prostheses lies in muscle group activations and the level of activation. These types of parameters are measured via the placement of the electrodes on the arm. The number of placement of electrodes and their size, amongst other parameters, have been the focus of the research in this field for the past couple of years [5]. Particularly, studies have shown that, although the level of accuracy using larger number of electrodes has increased, it has not increased significantly [5]. The common framework for the application of the acquired EMG signals is

via pattern recognition. [8], [9]. The classifier, built from pattern recognition, must be able to assimilate the information, interpret it and produce an outcome, ([9]), that is, it must decide which movement does which pattern of information it resembles.
There is a variety of classification approaches for EMG, each of them with their advantages and disadvantages. The following examples follow the overview established by Yousefit et al. [10]

- **Artificial Neural Networks (ANN):** The biggest advantage of ANN is their ability to learn from examples and their tolerance to vagueness. Due to this fact, they have been widely applied in the pattern classification of EMG. The computational method was created by Warren McCulloh and Walter Pitts in 1943 [11]. There are several types of techniques in the application of ANN, such as Hebbian Learning, backpropagation, convolution networks, amongst other types, all of which have been applicable in the classification of EMG systems [10]. Most of the problems stated with this type of algorithms deal with the fact that they require a lot of training data in order to perform acceptably in a real-time environment.

- **Support Vector Machine (SVM):** Support vector machine was introduced by Vapnik in 1963 [12]. Only recently SVM has started to be used in order to classify EMG signals for two main reasons: first, they are relatively more recent than the rest of machine learning algorithms, and second, they require more computational effort. Recent studies have shown that SVM classification outperforms linear methods and ANN systems. On the other hand, their applicability in real-life situations is limited. Their application has not only been shown for the detection of movement for robotics applications, but also for the detection of neuromuscular disorders.

- **Linear Discriminant Analysis (LDA):** LDA was first introduced by Rinald Disher in 1936 and, similarly to the Principal Component Analysis (PCA), it aims to reduce the dimensionality of data in order to increase separation of classes. Opposite to PCA, LDA looks to reduce dimensionality while increasing class separability of classes. In order to do this, LDA makes a set of assumptions which allows its applicability in computer systems to be simplified and to require very low computational level, making this an extremely attractive algorithm for real-life EMG pattern classification. It requires low level of training and reaches acceptable levels of classification accuracy.

2.2 Conclusion

In this project the focus lies in the limitations of myoelectrically controlled prosthesis. As it was possible to see through the course of this state of the art, there are limitations inherent to the cost of prosthesis itself, as well as, the softwares that have being used to control the same.

In the development of this project the focus will be given in the economic limitations of electrodes, particularly, with the advancements of 3D printing and the availability of new materials, this may come as a possible solution for this problem.

In order to test the applicability of a 3D printed electrode, a few algorithms will be placed in order to test for the classification performance of this material compared to the gold standard AgCl. Emphasis will be given to the LDA and SVM, the first because its has relatively good performance and can be placed in portable devices (i.e. prosthetic hands), and the latter one for its robustness.

Chapter 3

Material Properties

3.1 Introduction

The development of this project will ultimately rely on the development of 3D printed electrodes that will be used to gather myoelectric signals. Since a high impedance electrode is not useful as it is not able to conduct any signal, the proper development of these lies in the understanding of the material, and how the manipulation of the printing settings will affect its electrical conductive properties.
In this chapter, impedance spectroscopy measurements of the structures with the same overall shape but with different printing techniques and sizes will be presented. More specifically, the variation of parameters between structures such as the height of each layer during printing but also the type of infill, will provide insight regarding how the printing characteristics change the electrical properties of the material. Furthermore, the change of the size in between structures, while maintaining the printing characteristics constant, will provide insight with regard to the materials conductive properties.

3.2 Printing Properties and Material Conductivity Analysis

3.2.1 Methodology

The Setup

The electrical properties of the material were studied using an an LCR meter (HP 4284A) [13] in a two point measurement configuration. The measurement setup (as can be seen in figure 3.1)was composed of two wafers coated with 150 nm of platinum - the choosing of this material is mainly due to the fact that they do not oxidise with time. Impedance spectroscopy

is a major tool in analysing solid state dielectrics. The concept of this technology is to measure the impedance of the structure over a large range of frequencies. The ultimate goal of this technology is to gather information regarding the capacitive and resistive behaviour of the system. It can also provide information regarding electron transfer rate inside the structure giving information about ion mobility.

Each one of the platinum coated wafers has a soldered connection to the LCR, and AC voltage is applied to the bottom wafer whilst the readings are performed by the top wafer. The measurement commands (e.g, frequency range, sweeps, integration time...) are set up in Matlab and the connection between MatLab and the LCR is made via a GPIB-USB-HS (National Instruments, US) connection. The measurement specifications for the LCR are specified in Table 3.1.

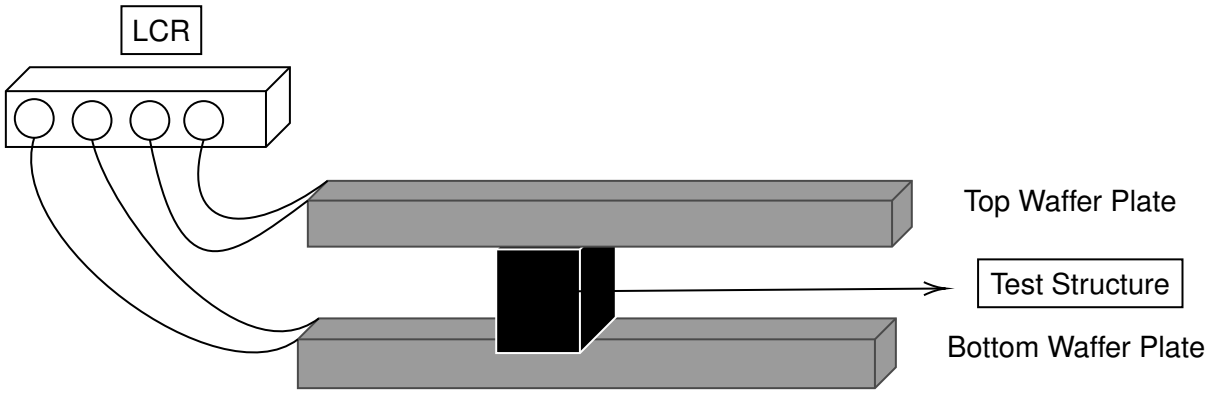

Figure 3.1: Scheme of the measurement Setup

Measurement Setting	Value	Description
Minimal Frequency (Hz)	20	Frequency at which the measurement starts and ends.
Maximal Frequency (Hz)	100	The lower limit of the LCR is 20Hz and the upper limit is 1MHz.
Sweeps	3	Each sweep is the running of the frequency spectrum (min to to maximum) one time. By performing several sweeps, its possible to gather more than one impedance measurement for all the frequency points. The final curve will presented by doing an average (per point) over the entire frequency band.
Measurement Voltage (V)	0.01	Applied voltage in the wafer electrode plate in order to perform the impedance measurement.
Bias	0	Option in order to apply DC voltage during the measurement procedure

Table 3.1: Measurement Specification in the LCR

The Test Structure

The structure in question is a cube fully printed using Pi-ETPU-250 (Palmiga Innovation, Sweden), the shape was chosen with this geometrical configuration due to its easy printability and consistent dimension in the X-Y direction. Furthermore, given the overall shape of the structure, it is easy to place it in the measurement platform. Particularly in this section of

the project, the goal is to look at how the printing settings can change the impedance measurement of the structures. In 3D printing there are a lot options that can be tweaked in order to print a structure. Figures 3.2 and 3.3 present a slicer view of the same structure with two different infills. Looking outside of the infill, in the same figures, it is possible to see two outer lines, which are called perimeter shells. Furthermore, the printing process is done through layers. The thickness of these layers can also be changed. Another parameter that can also be specified is the number of top and bottom solid layers. In this situation in particular the goal is to print fully infilled structures in order to better attest to their conductive capabilities but that is not always the case. If the infill is not meant to be 100%, top and bottom solid layers can be added in order to ”hide” the lower infill of the structure. In this project, these will be specified to a value of 3 for two main reasons. First because they help guarantee a better infill of the structure, as well as the printing consistency along the Z-Axis for the structure. Figure 3.4 presents the test structure used to perform all the measurements that will be described along this chapter. Furthermore, unless mentioned otherwise, the printing specifications of the test structures used in this chapter are the ones presented in table 3.2.

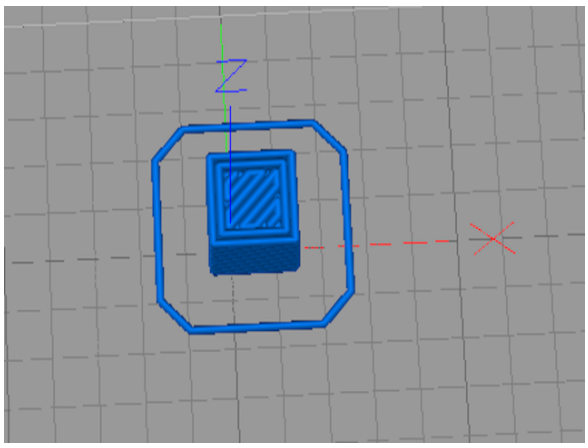

Figure 3.2: Structure 2

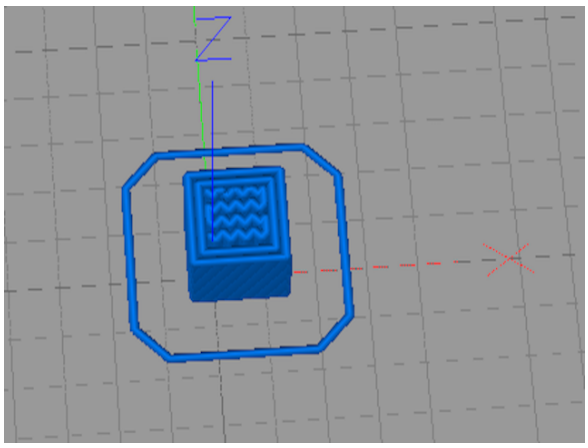

Figure 3.3: Structure 3

Following the printing settings presented in table 3.2, all structures were printed and the impedance spectroscopy was performed. The first structure was placed in the measuring plate and the location was marked. This was done to ensure that the following structures would be placed in the same location. Each structure was measured in the LCR following the guidelines of Table 3.1. Figure 3.5 shows how the overall setup in place during the measurement process.

Before the measurement procedure, both electrode plates, as well as the test structure, were cleaned with alcohol and dried. When manipulating the structures, latex gloves were used in order to prevent oils and unwanted particles from the user's hands from affecting the

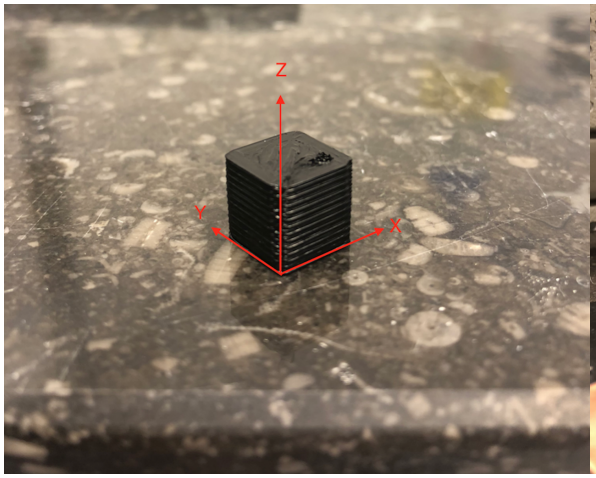

Figure 3.4: Test structure

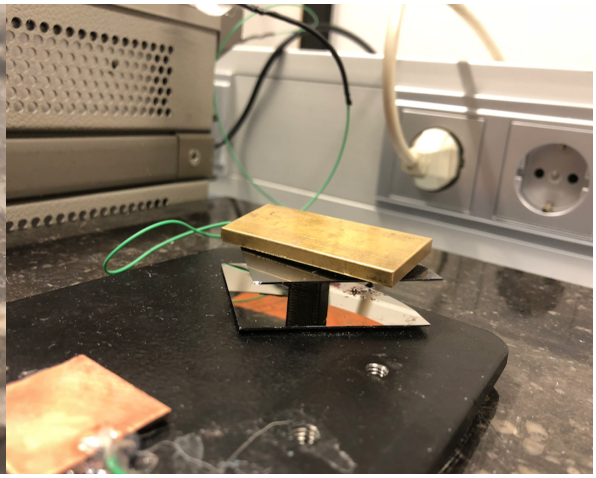

Figure 3.5: Measurement placement

measurement. Furthermore, if the measurement needed to be redone, the sample was not replaced by a new one, and the measurement leads of the LCR were not shielded.

3.2.2 Results

Layer Height Results

Figure 3.6 shows the results of the plots obtained from analysis of structures one and two. As it can be seen, when using a layer height of 0.1 mm there is a clear increase of impedance. Overall, the impedance of both structures is comparable, and the biggest difference verified between both structures was $1.7K\Omega$. Putting this into perspective, this value is 50% of the maximum value verified in the impedance measurement of the structure with the layer height of 0.2 mm.

Infill Pattern Results

Figure 3.7 shows the results of the comparison between two different infill patterns. Results show that the change of the infill into a *Full Honeycomb* has lead to the increase of the impedance results of the structure. The biggest difference between the two structures is $2.4K\Omega$ and when comparing this value to the impedance values of the grid infill structure, we see that the impedance of the *full honeycomb* structure is almost double. Furthermore, it is possible to see that the level of decay in impedance across the frequency range is similar for both structures.

Printing Specefications	Structure 1	Structure 2	Structure 3	Structure 4
Size (mm)	10x10x10	10x10x10	10x10x10	10x10x5
Layer Height (mm)	0.2	0.1	0.2	0.2
Infill Pattern	Rectangular	Rectangular	Full Honeycomb	Rectangular
Nozzle Temperature (ºC)	230			
Bed Temperature (ºC)	50			
Infill Percentage (%)	100			
Extrusion Multiplier	1.25			
Nozzle Diameter (mm)	0.8			
Top/Bottom Solid Layers	3/3			
Perimeter Shell	yes			

Table 3.2: Detailed presentation of the printed structures used and the printing properties used.

Total Electrode Height Results

Figure 3.8 presents the results from the impedance comparing two identical structures with different heights. As the results show, the structure with 10 mm presents a lower impedance when compared to the structure with a total height of 5 mm. Furthermore, the maximum difference verified between both structures is more than twice the maximum verified impedance for structure with 10 mm of height.

3.2.3 Discussion and Conclusion

Figure 3.6 has shown that the decrease in the layer thickness, which implies the increment of total number of interfaces between layers, results in a significant increase of the overall impedance of the structure. Moreover, changing the infill pattern of the structure from grid to full honeycomb has presented to have a significant impact on the impedance of the structure as well. It is important to note that there were more infill patterns available, but given the need to have a complete 100% infill structure, it was not possible to assess all of them as the infill condition could not be met due to printing limitations. Looking at the slopes presented by the two graphics, it is also easy to see that, when changing the infill of the structure besides the increase in impedance, it can be observed that the shape of the curve seen on the graph is somewhat similar for both structures. On the other hand, when the layer height of the printing was varied it is possible to see that the shape of the curve is not the same. Specifically, the decrement in layer height lead to the a more flattened curve in the impedance spectroscopy measurements.

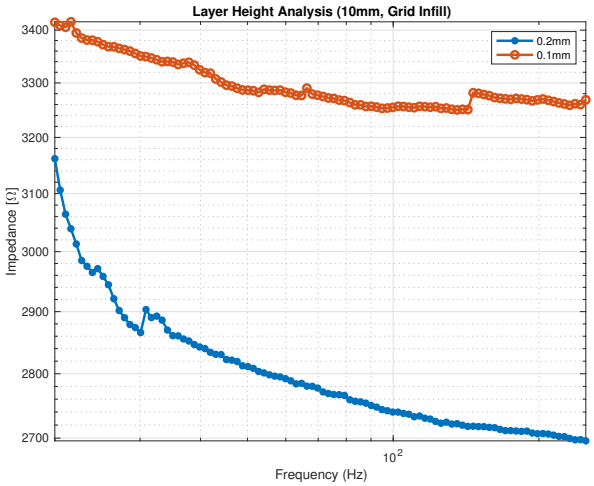

Figure 3.6: Comparison of Structures with different layer heights.

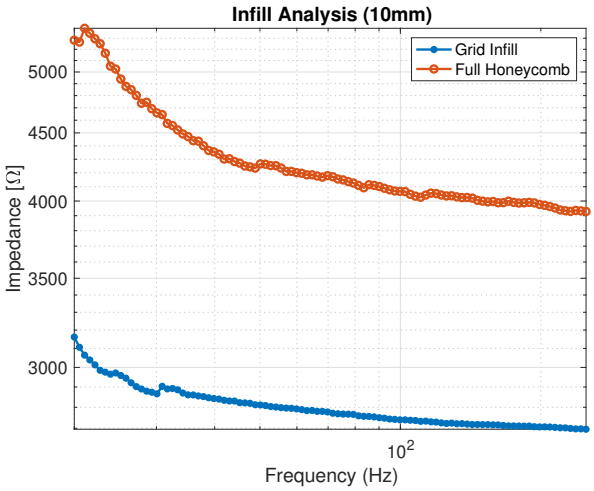

Figure 3.7: Infill Pattern Results.

The results of the change of the overall height of the structure from 10 mm to 5 mm were contrary to intuition. According to what was found in the two previous results and taking into account the total height of the structure it would be expected that the structure with the smaller height would present the smaller impedance as well. This makes sense since for half of the height as the 10 mm structure and with the same layer height, there are half the number of layer (as well as interfaces) and, as such, one would expect the impedance to be smaller as well. This is contrary to what the results have shown and the explanation for this factor is still uncertain. One of the possibilities found is that in fact the 100% infill condition for this project is not being met. Another possibility is that there is a variability between the printing of structures, which in turn lead to different results between structures.

This preliminary set of results has shed a preliminary light on how the printing settings affect the impedance of the structure and has risen more questions. On one hand, it is automat-

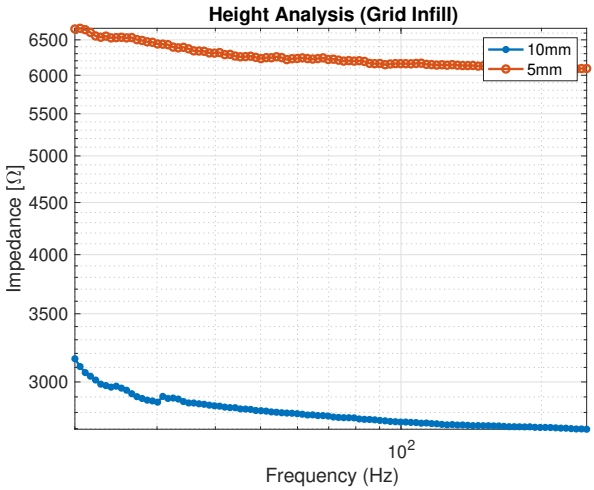

Figure 3.8: Layer Height Results.

ically possible to assess that the smaller the layers used in the printing setting, the higher the impedance measurements obtained, and it is believed that the cause of this in the resistance that charge suffers in crossing layers of the structure. Furthermore the infill has an effect in the impedance measurement of the structure although the reason for this is not completely understood. On the other hand, results regarding the impedance measurement of the structure have shown to be contrary to the first argument set in this paragraph. This raises questions regarding the printing consistency amongst other factors.

3.3 Printing Consistency

Particularly one of the results from the previous section rose questions regarding the printing consistency. In this section, a methodology was set in place to check the statistically significant variations in impedance spectroscopy measurements of structures that are printed using the same printing settings.

3.3.1 Methodology

Seven identical structures and identical to structure number 4 from Table 3.2 were printed in two different batches making a total of 14 structures printed. The test was conducted by comparing the results inside the same batch of printed structures as in between batches as this would give us two important informations. First, if there was a difference between structures printed in the same batch. Second, if there were differences between batches printed.

The position of each structure printing bed was given a number as well as an extra number to set the batch at which it belonged (e.g. 11 for the structure from batch one in position one). Each electrode was measured once and the measurement settings of the LCR are presented in Table **??**.

Measurement Setting	Value
Minimal Freq (Hz)	20
Maximal Frequency (Hz)	1000
Sweeps	3
Measurement Voltage (V)	0.01
Bias	0

Table 3.3: LCR Specifications for Long-Time Measurements

3.3.2 Results

Figure 3.9 presents the results of the maximum difference between electrodes verified at each point acquired over the frequency range. At each frequency point it is possible to see the maximum difference observable between structures, and this is the value that is being plotted in the graphic. The biggest measured impedance across 14 structures was 8.7$K\Omega$. It is clear from this graph that batch one presents, overall, less differences across the entire points acquired when compared to batch number 2. These conclusions are reinforced by the results presented in Figure 3.10, where it is clear that, for batch one, the mean is close to zero for the maximum observable difference, with some outliers measurements. On the other hand, for batch two, the mean for batch two is around 200 Ω and with a higher number of outliers.

Figure 3.11 shows the results of the two batches. In each point, the impedance measurements of each sample for that frequency are averaged over all the acquired points and the standard deviation between those is calculated in order to plot the error bars. As it possible to see from the plot presented, the average of the impedance between the two batches is comparable at around 4$k\Omega$. On the other hand, the measurement of the structures inside the same batch present a higher standard deviation, especially in the lower frequency component.

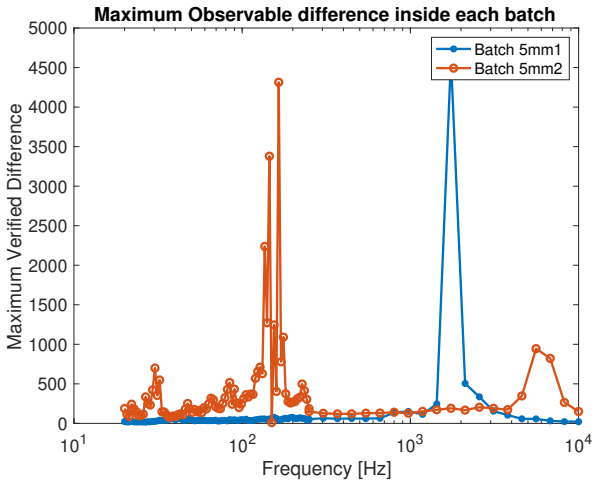

Figure 3.9: Maximum verified difference between electrodes inside the same batch.

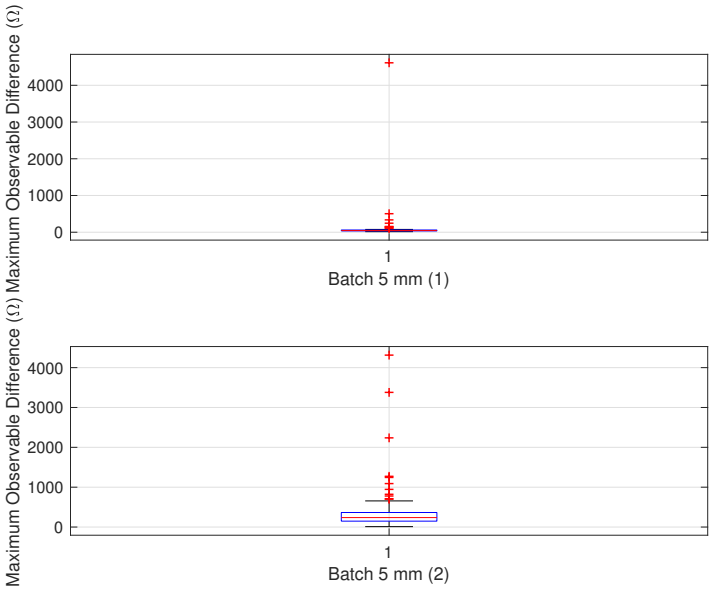

Figure 3.10: Boxplot of the maximum verified difference of impedances inside the same batch

3.3.3 Discussion and Conclusion

Figure 3.9 compares each electrodes to its counterparts inside the same batch. As it is possible to see, particularly in batch number 1, there are no differences between impedance measurements inside batch one as the different values are, for the majority of acquired points, close to zero. Despite the fact that batch number two presents a higher number of points at which the difference is not zero, it can be seen that the printing position has no effect in the impedance properties of the structure, hence, it does not induce variability in

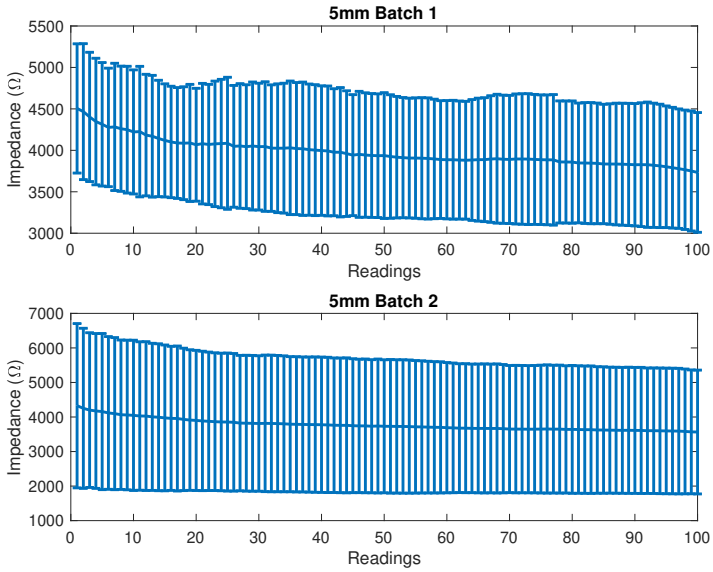

Figure 3.11: Comparing batches

the results of printed structures.

Figure 3.11 it is possible to see the mean and standard deviation of impedance measurements at any given frequency point for the two batches. As can be seen, the average of the impedance measurement is comparable for both structures. Despite this fact, it is possible to see that the standard deviation between values is not negligible, which in turn raises questions regarding the reproducibility of the results. This lack of consistency in the measurements observed in the large value of the standard deviation inside the same batch can have two possible sources. First, since the standard deviation values seem relatively larger in the low frequency component, it is possible to assume that the measurement procedure is inducing alterations in the material properties, which in turn is affecting its electrical conductivity capabilities. Another possible explanation lies on the way the setup itself was done.

3.4 Impedance Measurement Over Different Directions

The previous set of results have shown that the printing position of the batch is not affecting the impedance spectroscopy of the structures. However, there are clear inconsistencies due to the high values in standard deviation of the measurements. These can be explained by the way the setup is mounted or it can be explained by the act of measuring.

The logic behind the following sets of measurements is the following: The structures are identical along the Z-direction, which means that impedance measurements with the structure in an up straight position or facing down should, in theory, return approximately the

Printing Specifications	Printed Structure
Size (mm)	10x10x10
Layer Height (mm)	0.2
Infill Pattern	Rectangular
Nozzle Temperature	210
Bed Temperature	45
Infill Percentage	100
Extrusion Multiplier	1.25
Nozzle Diameter (mm)	0.8
Top/Bottom Solid Layers	3/3
Perimeter Shell	Yes (2)

Table 3.4: List of printing specifications for Pi-ETPU-700+

same impedance measurements.
Up to this point, due to the low familiarity of the user with AM all tests had been performed with Pi-ETPU 250. From this point onwards, the printing was performed with Pi-ETPU 700+ which is the same material but with a higher level of graphene. Because of that the printing settings had to be slightly changed in order to match the specifications of the new material.

3.4.1 Methodology

Three structures were printed following the new printing guidelines presented in Table 3.4. After the printing, one set of impedance spectroscopy measurements was performed in each strcuture. The measurement settings of the LCR are the same as before and are given by Table **??**. Each structure was measured once on a different direction (one in the normal position, another one upside down and the latter placed on the lateral side). As with the previous structures, the new material was handled with gloves as well in order to prevent oils and dirt from the hands from affecting the structure. Furthermore, previous to the measurement itself, both the wafer plates and the structure were cleaned with alcohol. Once the alcohol naturally air-dried, the structure was placed in the measuring plate and the measurement started.

3.4.2 Results

Figure 3.12 presents the results for the impendace spectroscopy for each of the identical structures measured on a different position. It is possible to see that there is a significant discrepancy between the impedance measurements between the normal and the upside down position. Furthermore, with the new impedance, measurements are oscillating a lot in the low frequency component. Additionally, the lateral impedance measurement is significantly lower (approximately 80% lower when compared with the electrode in the upside down position) than the other two performed.

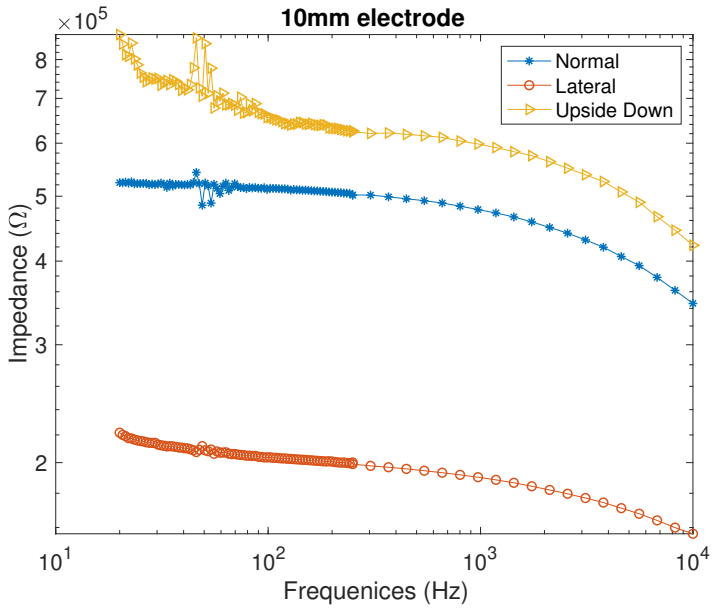

Figure 3.12: Measurements of a 10 mm structure at different positions

.

3.4.3 Discussion and Conclusion

As it was introduced in the introductory section of this section, one of the things to be expected from this set of measurements was that the impedance measurements in the normal and the upside down positions of the cube would return approximately the same range of values. This is not verified by the results - in fact there is a discreancy of more than 30% between the normal and upside down reading. This can't be explained by printing problems, as it was discussed earlier that these should not have significant influence in the measurements and, as stated as well, the structures are identical in the Z-direction.

In the development of this research, and also due to the change in the material infill, a lot irregularities were found in the measurements, especially in the low frequency component. After looking at the LCR manual [13], it is likely that this is due to the fact that the impedance

measurement was falling outside of the range of the LCR due to the voltage that was being applied during the measurement. Figure 3.13 shows the measurements performed in one of these structures but at different voltages. It was possible to assess that the measurement was being performed at an improper voltage which was also returning wrong impedance measurements from the LCR.

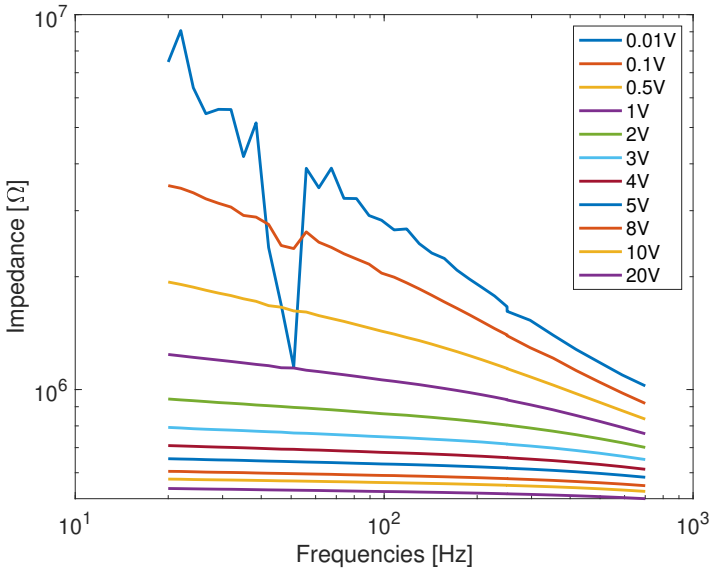

Figure 3.13: Measurements of a 10 mm structure at different voltages

.

All in all, the measurements performed have shown that, first, the origin of the discrepancy between results in the normal and the upside down measurements is not fully understandable yet, and given that the structure presents no difference along the Z-Axis the results have been pointing to the fact that the inconsistency comes from the measurement setup itself. Furthermore, the results have pointed out that the measurement settings need to be changed, particularly the Voltage of the LCR.

3.5 Long-Time Measurements

In chapter 3.4.3 it was mentioned that there were problems that were verified in the new sets of measurements. These problems are associated with either the measurement setup or with the measurement process itself that could be altering the physical properties of the material. In order to answer de second question, the following methodology was set in place.

3.5.1 Methodology

In order to see if the measurement time would have an effect in the impedance of the structure the following was set in place. The new structure (with the same parameters a structure 2) was printed to make sure that previous measurements would not have affected the physical properties of the material. The LCR settings for acquiring data over the course of the following measurements are presented in Table 3.5 Following the end of the first 6 hours of data acquisition, the structure was left for 2 hours, and then another two hours of consecutive measurements were performed. The point of this last measurement was to find whether the structure would be altered by the measurement procedure, or if it would return to the original state after some time.

Measurement Setting	Value
Minimal Freq (Hz)	20
Maximal Frequency (Hz)	1000
Sweeps	Not Applicable
Measurement Voltage (V)	3
Bias	0

Table 3.5: LCR Specifications for Long-Time Measurements

3.5.2 Results

Figure 3.14 and 3.15 present the 6 and 2 hour- long-time measurements. It is important to note that before this exercise I was unable to fully reach 100% in the printing structures. For this reason, the impedance values of the long time measurements are higher than the ones presented before. Furthermore, as it possible to see in the figures, the impedance of the measurement drops with the measurement process. First, for the six hours of continuous measurements, we can see that the impedance (for the 20 Hz measurement) dropped from 365 $K\Omega$ to 360$K\Omega$. After the two hour measurement a drop from 356$K\Omega$ to 354$K\Omega$ is observed.

3.5.3 Discussion

As it can be seen from the results presented, in the first 6 hours of measurements the overall impedance of the structure fell from 365 $K\Omega$ to 360 $K\Omega$ and in the two hour measurements it dropped from 356$K\Omega$ to 354$K\Omega$, which equates to a drop in impedance of 1.6% and 0.5%,

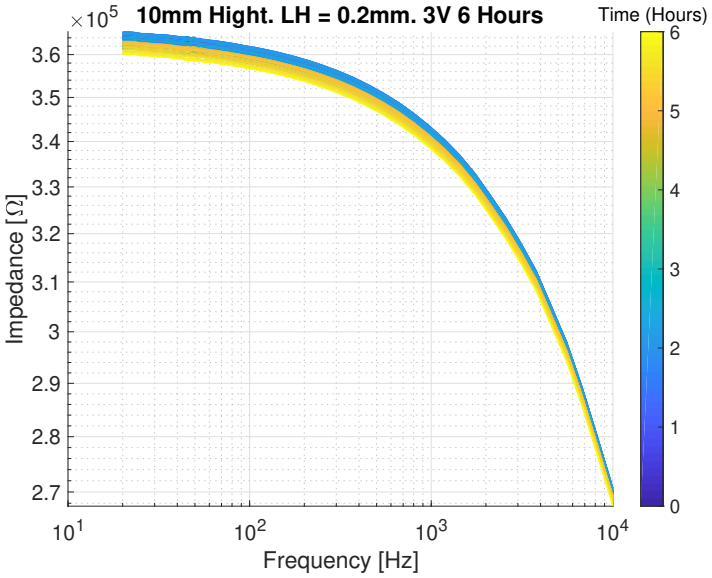

Figure 3.14: Long time measurements results for 6 consecutive hours.

respectively. This means that, although in fact the impedance measured drops through time, the changes in the material properties cannot be explained as after 6 hours of measurements the values obtained in the second set of measurements are comparable to the first, and the drop in impedance is not significant.

One possible explanation for this would actually be the decrease in contact resistance between the electrode plate and the structure. Since the top electrode plate is balanced on top of it, sometimes due to printing limitations as seen in figure 3.4 the structure is not completely flat on the surface, which may lead to higher contact resistances that what would be normal.

3.6 Electrode Design Insights

Over this chapter a series of experiments were presented to give insight regarding the material properties and how the impedance of test structures alters by varying printing properties. Overall, a point was reached where the main insights regarding the design of electrodes were made possible.

There are still plenty of questions that have arisen from this section. Particularly, it was not fully understandable how the current propagates inside the structure, and if the shape could potentially affect significantly its electrical properties. What we can conclude from this is that there should be a compromise between electrode size and its impedance.

What is understood, is that in order to decrease the overall impedance of the structure, the

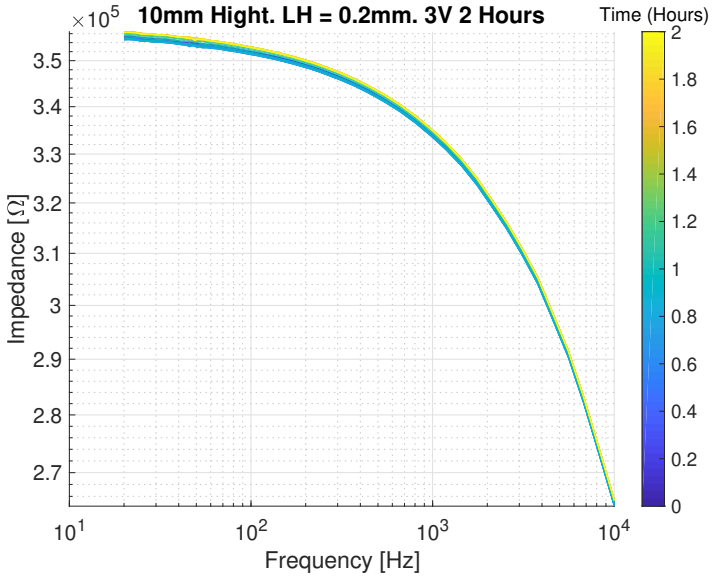

Figure 3.15: Long time measurements results for 2 consecutive hours.

number of interfaces across the X-Y-Z interface should be decreased as much as possible.

3.7 Conclusion of the Chapter & Future Insights

In the beginning of this chapter, the goal was set out to retrieve insights from the impedance spectroscopy measurements regarding the tweaking of the printing settings in order to decrease, as much as possible, the impedance of a Pi-ETPU based structure. Furthermore, the insights provided by these measurements should give sufficient insight on the physics of the charge conduction inside the material. First and foremost, from the first measurements performed, it is easy and intuitive to understand that it is necessary to minimise the number of interfaces in the printed structure, as it so appears that charge suffers a hight amount of resistance in crossing this interface. Furthermore, it is understandable that the infill of the structure also has an effect in charge conduction inside the structure, but it is not fully understood why.

One of the recurrent problems presented along this chapter relates to the reproducibility of results, especially in the low frequency component. Long time measurements have disproved the theory that the material properties were being changed by the measurement procedure. On the other hand, the discrepancy of results between the normal and the upside down results in Figure 3.12 points to a need to change the measurement setup. Some trials were performed by trying a 4-point measurement through the placing of pins in the structures but, due to the hight level of density of the structure, this was not possible to

achieve. Furthermore, taking into account the remaining objectives of this project, the setup was not improved.

Chapter 4

Electrode Design and Analysis

4.1 Introduction

The previous chapter gave insights on the influence of printing techniques on electrical impedance. In this chapter, the goal is to print two different shapes of Pi-ETPU-700-based electrodes based on the insights retrieved from the previous chapter. Following this, impedance spectroscopy of each of these will be performed and compared to standard AgCl electrodes. Last but not least, a fitting of a model of the data acquired will be performed.

4.2 Design

Two electrodes shapes were designed following the SENIAM guidelines for electrodes size ([14]). More particularly, the guidelines state that for circular electrodes the diameter should not exceed 10 mm, and for other shapes they should not have a length superior to 10 mm in the direction of the muscle fibre. Figure 4.1 presents the CAD design of a circular electrode and figure 4.2 presents the CAD design of a rectangular electrode, and both electrodes were fitted with a structure that would allow for a Snap-Button connection for two main reasons: first, the device that will be later used to perform EMG readings uses this type of connector; second, snap-button connectors are still an industry standard for their reliability and for providing a stable connection. Table 4.1 presents the size and the printing specifications of both electrodes, and the electrode itself is composed of Pi-ETPU and the supporting structure surrounding it is composed of NinjaFlex. This material was chosen due to its non-conductive and flexible properties.

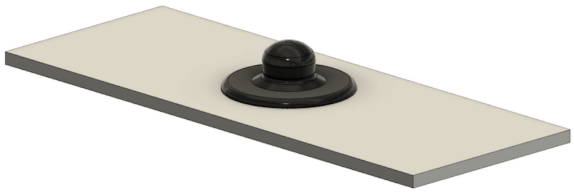

Figure 4.1: Design 1

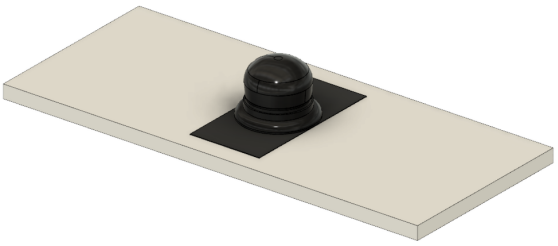

Figure 4.2: Design 2

Printing Specefications	Design 1	Design2
Size (mm)	d = 10; h = 1	10x5x1
Layer Height	0.200	
Infill Pattern	Rectangular	
Nozzle Temperature (ºC)	208 (Pi-ETPU) 230 (NinjaFlex)	
Bed Temperature (ºC)	45	
Infill Percentage (%)	100	
Extrusion Multiplier	1.3 (Pi-ETPU) 1.2 (NinjaFlex)	
Nozzle Diameter (mm)	0.8 (Pi-ETPU); 0.6 (NinjaFlex)	
Top/Bottom Solid Layers	3/3	
Perimeter Shell	2	

Table 4.1: Printing specifications of the electrodes

4.3 Impedance Spectroscopy

4.3.1 Methodology

The impedance as a function of frequency of the electrodes was measured using an LCR meter (HP 4284A) in a two point measurement configuration. One of the connections is soldered to a platinum wafer onto which the electrode is positioned (similar to what was presented in 3.2). AC voltage is applied to the wafer and the reading is done by a snap button, which is soldered to the second connection of the LCR, and connected to the electrodes whose design was presented previously. The measurements are made in the entire range of frequencies of the LCR (20Hz to 1MHz) at 3V with no bias (A full set of the LCR parameters is present in Table 4.2).

Measurement Setting	Value
Minimal Freq (Hz)	20
Maximal Frequency (Hz)	1 000 000
Sweeps	Not Applicable
Measurement Voltage (V)	3
Bias	0

Table 4.2: LCR Specifications for Long-Time Measurements

4.3.2 Results

Figure 4.3 presents the results of the impedance measurement. As can be seen from the plot, the impedance of both the Pi-ETPU electrodes is similar whilst, as expected, the impedance of the AgCL based electrode is significantly lower.

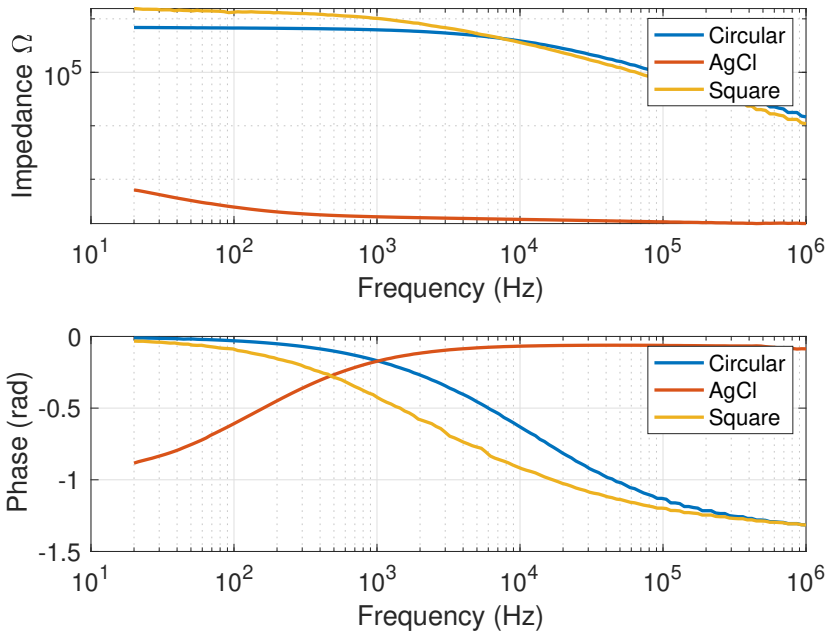

Figure 4.3: Impedance measurement results.

4.3.3 Discussion and Conclusion

One can see from figure 4.3 that there is a significant difference between the overall impedance of the Pi-ETPU and the AgCl electrodes. Looking at the measurements of both the circular and the square electrodes, the area under the curve of the square electrode is 3.9245×10^{10} HzΩ

whilst the area under the curve of the circular electrode is 4.8602 $\times$ 10^{10} HzΩ. Furthermore, when examining closely the plot (which is on a logarithmic scale), we can assess that the overall impedance of the square electrode, in the EMG frequency band, is almost twice as the circular one. Because of these measurements of the electrodes presented, it was determined that the subject EMG measurements would be performed with the circular electrodes.

4.4 Electrical Characterisation

Electrical characterisation of electrodes puts a physical mean in the observed data. Furthermore, this is an important step in modelling the resistance that the charge suffers while going through the electrode.

4.4.1 Model Fitting

The fitting of the model was done using Matlab's function "fminsearch", which uses the simplex search method of Lagarias (or Nelder–Mead simplex algorithm). The algorithm starts with an initial set of points arbitrarily determined that form a simplex. A simplex is a polytope in N dimensions with N+1 vertices, more specifically, in two dimensions a simplex can be seen as triangle. In each iteration, the algorithm determines the worst corner point of the simplex and attempts to replace it by introducing a new point, producing another simplex. The replacements are chosen by a series of operations such as reflexion, expansion, inside and outside contractions of the simplex, the algorithm is able to find a local minima of the function.

More specifically, this chapter will present physical models that attempt to explain the behaviour of the electrode, and the approximation of the model parameters will be done by minimising the value of the function presented in equation 4.1. Function f is a function dependent on the components that build the models that will be discussed, and these parameters need to be optimised in order to minimise the error between the data (y) and the predicted values using such parameters ($\hat{y}$).

After the determination of the parameters it is necessary to evaluate the quality of the fitted model to the real data. In order to do that, the root mean square deviation (RMS) was used, as this method is commonly used to evaluate differences between values of models and data. The equation, which is represented by the RMS present in equation 4.2, is where T represents the number of observations, y represents the electrode data acquired from the

impedance spectroscopy measurement and $\hat{y}$ represents the fitted data. The values of RMS were normalised in order to provide a better comparison between the three models.

$$f(R_{\mathsf{s}}, R_{\mathsf{p}}, C_{\mathsf{p}}, A) = \log(y - \hat{y}) \tag{4.1}$$

$$RMS = \sqrt{\frac{\sum_{n=1}^{T}(y_n - \hat{y}_n)^2}{T}} \tag{4.2}$$

4.4.2 Physical Models

Due to the overall composition of the electrode, the first models used to fit the impedance spectroscopy data to a physical model were the ones presented in figures, 4.4, 4.5, 4.6 . The electrical model 1 present in figure 4.4, was taken as a starting point for the model as this is the standard model in an electrode-electrolyte system [15].

Each model is composed of the following components:

- R_{s}, which represents the contact resistance between the electrode plate and the structure. It is the resistance the charge faces when leaving the electrode plate and entering the structure. R_{s} represents the contact resistance between the electrode plate and electrode.

- C_{p} represents de double layer capacitance between the electrode and the platinum wafer. The impedance of the capacitor is provided by equation 4.3. The charge transfer between two structures leads to the accumulation of charge on the interface. This factor is frequency-dependent and modelled via a capacitor.

$$Z_{\mathsf{c}} = \frac{1}{j\omega C} \tag{4.3}$$

- R_{p} represents the leakage resistance across the double layer. This resistance can be associated with imperfectly sealed configurations of bipolar electrodes which result in the leakage of current from electrode to another. In this case, the leakage would be from the platinum covered wafer to the Pi-ETPU electrode. [16]

- W_{a} represents the Warburg element. This model, much like resistances and capacitors, represents a resistance to charge transfer inside the electrode. However, unlike

these structures, the resistance produced by this element is frequency dependent, whereas the phase is constant at $\pi/4$. In [17] the author states that one of the possible physical meanings for the existence of the Warburg element is related to adsorption and mass transport. As we will see later in this chapter, the incorporation of this element is essential to properly model the electrodes. The impedance of the Warburg is given by equation 4.4.

$$Z_{\mathsf{w}} = \frac{A}{\sqrt{\omega}} + j\frac{A}{\sqrt{\omega}} \tag{4.4}$$

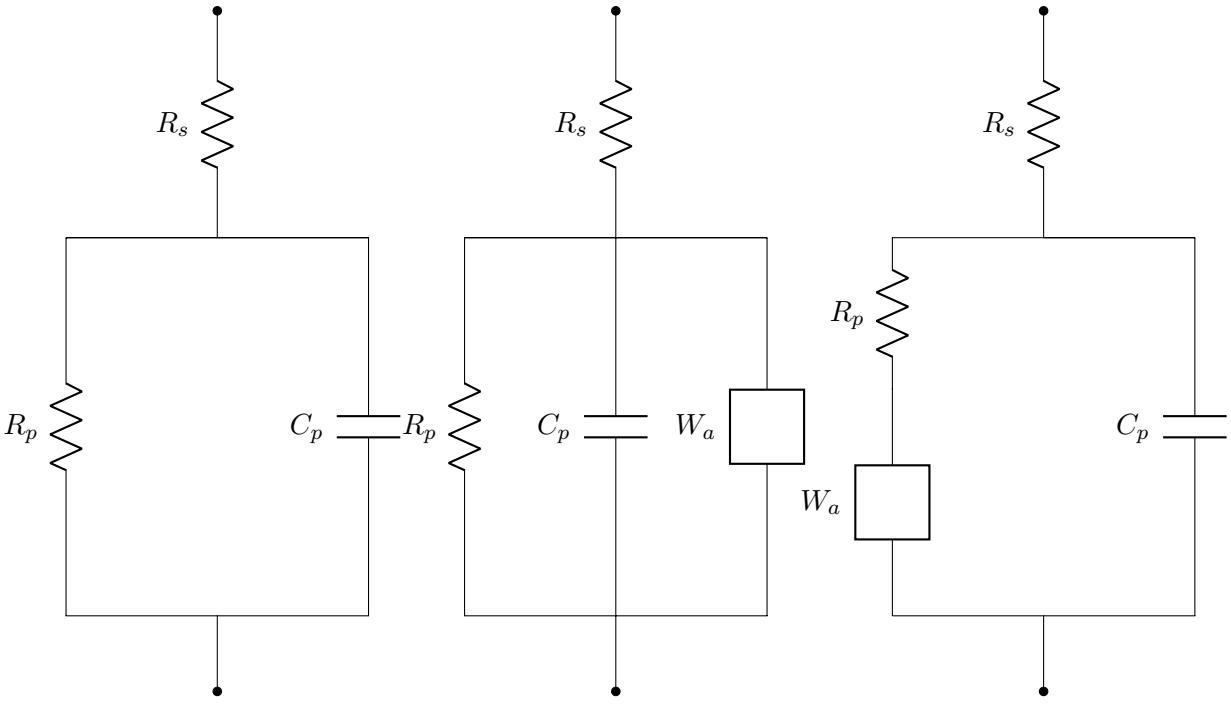

Figure 4.4: Model 1

Figure 4.5: Model 2

Figure 4.6: Model 3

In order to perform the fitting of the models, each model had to be simplified to one single equivalent structure, and all follow the exact same type of rules.

- In model 1 there is a resistance in series with a parallel element composed by a resistance and capacitance. The simplification of the parallel element is given by equation 4.5. By simplifying the first parallel element the equivalent circuit of model 1 is given by equation 4.6.

$$\frac{1}{Z_{eq1}} = \frac{1}{Z_c} + \frac{1}{R_p}$$
$$Z_{eq1} = \frac{R_p Z_c}{R_p + Z_c} \tag{4.5}$$

$$Z_{\text{model1}} = R_s + \frac{R_p Z_c}{R_p + Z_c}; \tag{4.6}$$

- Following the same logic as before, model 2's equivalent impedance is given by equation 4.7.

$$Z_{\text{model2}} = R_s + \frac{R_p Z_c Z_w}{R_p Z_c + R_p Z_w + Z_c Z_w} \tag{4.7}$$

- Following the same logic as before, model 3's equivalent impedance is given by equation 4.8.

$$Z_{\text{model3}} = R_s + \frac{(R_p + Z_w) Z_c}{R_p + Z_w + Z_c} \tag{4.8}$$

4.4.3 Results

Figures 4.7, 4.8 and 4.9 present the best results of fitting models 1,2 and 3, respectively, to the impedance spectroscopy measurements performed. The results for each of the components of the model are presented in the table 4.3.

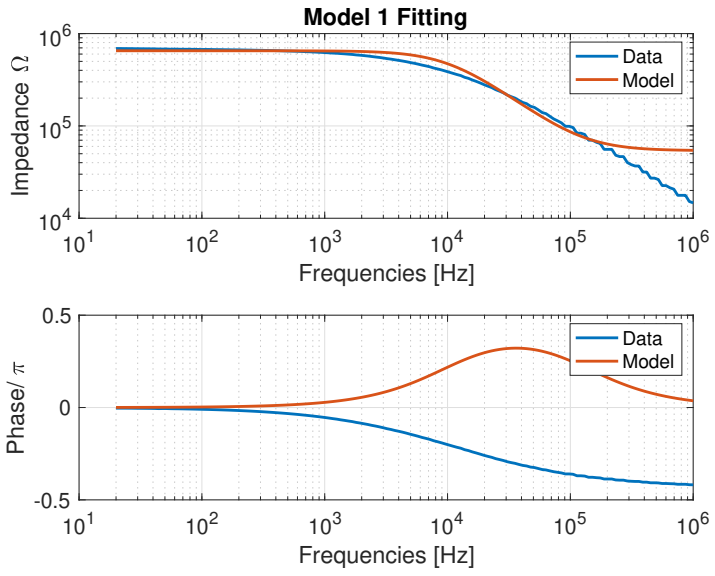

Figure 4.7: Model 1 Fitting Results

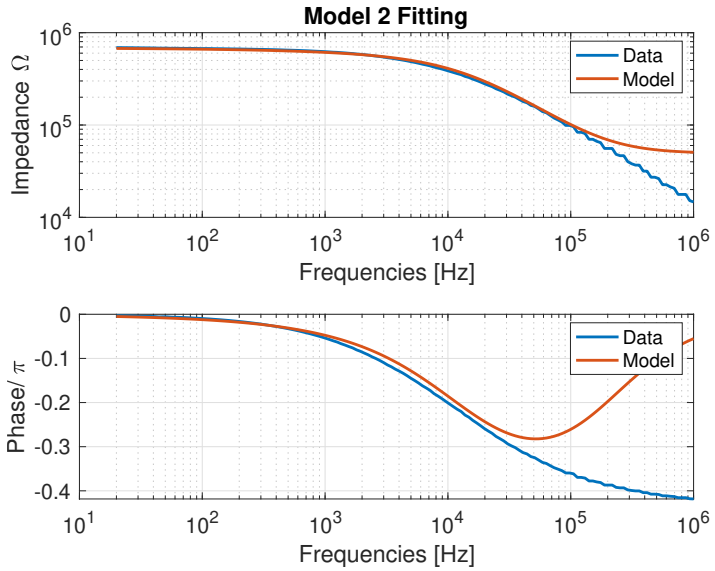

Figure 4.8: Model 2 Fitting Results

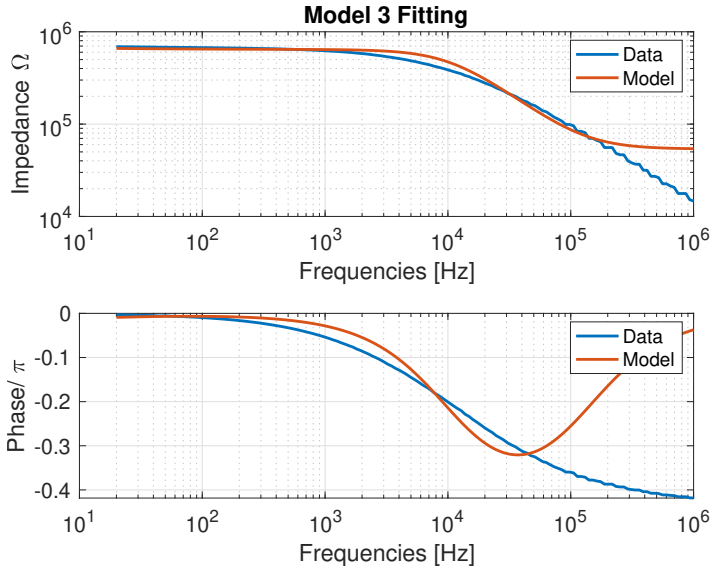

Figure 4.9: Model 3 Fitting Results

Component	Model 1	Model 2	Model 3
R_s (kΩ)	53.98	49.39	53.76
R_p (kΩ)	597.42	635.31	587.99
C_p (pF)	25.57	17.20	25.18
A (Units)	-	2.22×10^8	1.99×10^5
RMS	0.1061	0.0388	0.1012

Table 4.3: Summary of results from the model fitting

4.4.4 Discussion

During the impedance spectroscopy measurements, one of the first things that became noticeable in regards to the behaviour of the electrode had to do with the slope of impedance decay over the frequency range. When examining the electrode acquired data, it is possible to see that the impedance of the electrode starts to decay with a slope of approximately $\omega^{-0.5}$. Since a physical explanation for the behaviour of the electrode is required, this type of slope can not be modelled naturally through the sole use of inductors, capacitors and resistances. As touched upon in the previous chapter, there is not enough information regarding the material that allows to fully understand how it behaves, and because of that the Warburg element was introduced in models 2 and 3. Opposite to the resistors and capacitors, which model an ideal resistance to mass transfer, the Warburg element is more complicated. The physical meaning of the component is hard to derive, nonetheless, as the results have shown, this presents an essential component in the modelling of the behaviour of this material.

Figure 4.7 shows the fitting of model 1 to the impedance spectroscopy data. The RMS value is the highest between all of the three models, since it does not possess a component capable of producing the characteristic slope of the electrode. Furthermore, the behaviour follows the expected path.

Figure 4.9 presents the results regarding the fit of model 3, where the main deviation from model two is that the Warburg element is in series with the resistance instead of all elements being in parallel. The main difference from model 1, in the fitted data, is that this model is able to produce a better approximation of the modelled data in the high frequency components. Despite this fact, the corner frequency for the model does not match the one of the real data.

By placing all three components of the model in parallel (results presented in figure 4.8), the quality of the fit improves significantly across the low-mid frequency range. Furthermore, the corner frequency as well as the slope of the drop of the model matches the acquired data. For high frequency components the model stabilises at $\approx 50k\Omega$, and as for the high frequency components the impedance of both the Warburg element and the capacitor tends towards zero. The logic presented in equation 4.9 shows why the impedance of the capacitor and the Warburg element going to zero, and equation 4.10 shows how the only remaining of the high frequency component is the the value of R_{s}. Due to the equation 4.9 this remains true for all three models as expected.

$$\begin{aligned}\lim_{\omega\to\infty} Z_{\mathsf{c}} &= \lim_{\omega\to\infty} \frac{1}{j\omega C} = \frac{1}{\infty} = 0 \\ \lim_{\omega\to\infty} Z_{\mathsf{w}} &= A(1-j) \lim_{\omega\to\infty} \frac{1}{\sqrt{\omega}} \\ &= A(1-j)\frac{1}{\infty} = 0\end{aligned} \tag{4.9}$$

$$\begin{aligned}\lim_{\omega\to\infty} Z_{\mathsf{model1}} &= R_c + \lim_{\omega\to\infty} \frac{R_{\mathsf{p}} Z_{\mathsf{c}}}{R_{\mathsf{p}} + Z_{\mathsf{c}}} \\ &= \frac{R_{\mathsf{p}} \times 0}{R_{\mathsf{p}} + 0} = R_c\end{aligned} \tag{4.10}$$

Although the results that the previous approximations provided are satisfactory, it is possible to see that they do not resemble the true behaviour of the electrodes as both the phase and the impedance do not fit the data in the high frequency component. Because of this a manual fitting can be done in order to extract a better insight regarding the physics behind the electrical behaviour of the electrode. Furthermore, in order to get a comparison with the gold-standard, a manual fit for the AgCL electrode was also performed.

As the data shows, the AgCl electrode could me modelled initially as a series of resistor, capacitor and Warburg element. It is possible to clearly see that when going through the frequency component, initially the impedance drops with the slope smaller than ω (again, its not possible to model the behaviour only with a capacitor) and tends to stabilise in the R_{s} value when ω goes to infinity. The results of this fit are presented in Figure 4.10 and it is possible to see that they resemble the data quite specially in the lower frequency component.

In order to get the manual fit for Model 2, the values gathered from Table 4.3 were used as a starting point. Particularly, looking at the initial fit, it is possible to see that the contact resistance R_{s} is too high, since that the impedance keeps decreasing. Manipulating the results, it was possibel to reach the fit provided by figure 4.11. The results of each of the components of the models are provided in Table 4.4.

Overall looking at both models, there are clear differences one can expect from the signal acquired from the electrodes. If the attention is focused on the contact resistance R_{s}, it is possible to see that the Pi-ETPU electrodes has around 8 times more contact resistance than the AgCL one. This in turn will affect the level signal that will be acquired, and predictively more noise will be present in the Pi-ETPU based electrode.

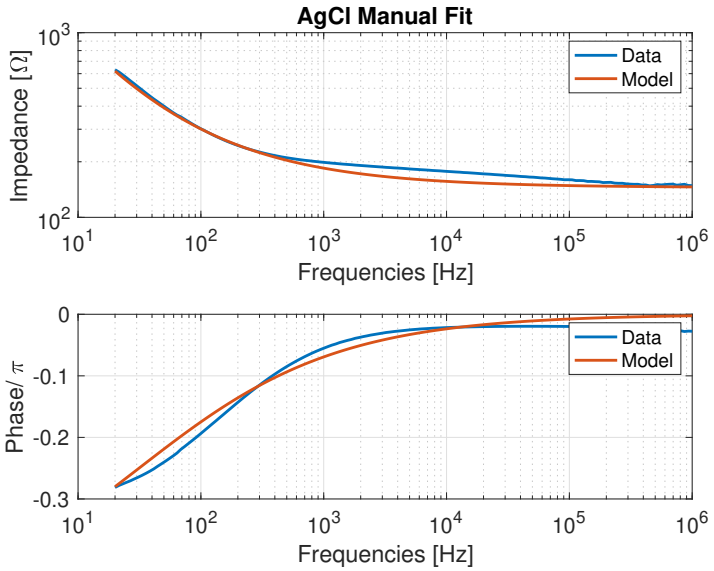

Figure 4.10: AgCL Manual Fit

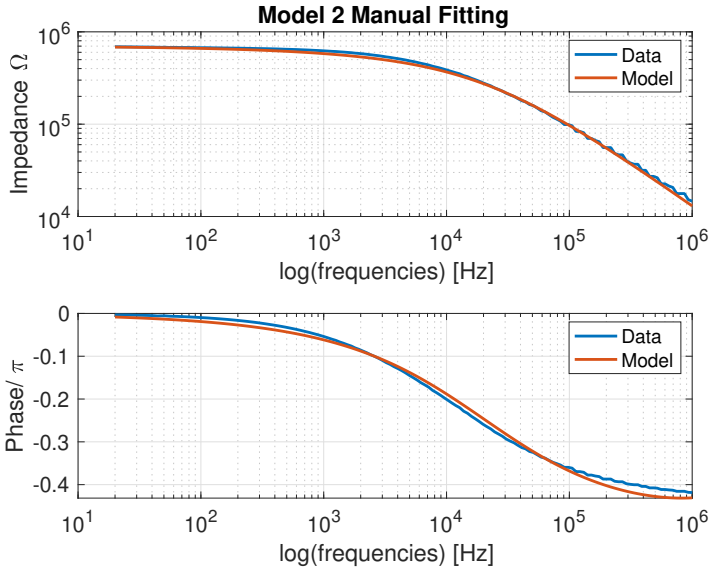

Figure 4.11: Model 2 Manual Fit

Component	AgCl	Pi-ETPU
Rs (Ω)	145	1200
Rp (Ω)	-	7×10^5
C (μF)	35	11×10^{-6}
A ($\Omega.s^{0.5}$)	2800	150×10^6

Table 4.4: Manual Fit Parameters

4.4.5 Conclusion

The goal of this chapter would be to compare two shapes of the Pi-ETPU based electrodes and gather insights regarding the conductive properties of one of this with the AgCl. Overall, impedance spectroscopy measurements of the two shapes of electrodes, have shown a lower impedance of the circular electrode compared to the square one, because of this, this one the one one chosen for future tests.
Overall via the manual fit, it was possible to reach a very good approximation of the physics behind the transfer of charge inside both structures. This has also set the way, to get a preliminary idea how the quality of the signal will differ between the two electodes.

Chapter 5

Electrode Functionality Analysis

5.1 Introduction

Electromyographic signals possess a lot of information regarding both contraction intensity and the type of movement that the user is performing. The problem with using these types of signals to control assistive devices lies in the complexity of the signal. First, when recording EMG from the surface of the skin, the electrode is, in fact, recording the EMG signals of a group of muscular fibres. As fibres and motor units depolarise, the recording of the signal is in fact the superimposition of several signals. Second, there is a variety of factors that will affect the quality of the signal. Some examples are the inherent noise associated with electrical equipment, motion artefacts, amongst other possible causes [18]. This entails that the signal needs to be decoded and simplified in order to be analysed.

Figure 5.1 presents the pipeline that was implemented in this project. In this project, a pattern recognition algorithm (classifier) is built with pre-made recordings during offline training. After that, in online mode, the same pipeline follows an online path, but the classifier is able to determine the gesture that the user is doing in real time. In this section, each component of the pipeline will be presented and its theoretical incorporation explained. Each of these components were coded in MatLab 2018a and implemented in a user interface. The goal of using this lies in the simplification of the data acquisition (both for the subject as well as for the scientist) when performing studies associated with EMG signals. Up to the point of the finalisation of this project, the GUI was built in order to support up to 7 movements, automatically build a machine-learning method (a classifier), perform an online test of the classifier, and provide a connection to a robotic arm. This last section was not tested and falls outside the scope of this report.

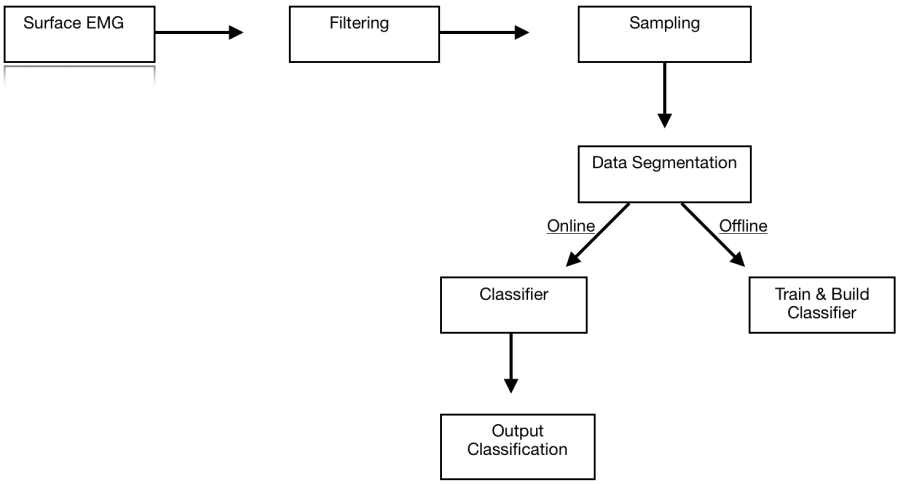

Figure 5.1: Pipeline from signal acquisition to classification

5.2 Data Acquisition

EMG signals are retrieved using a 16-Channel Refa (TMSi, Oldenzaal, NL) [19] through a MatLab interface custom-built for this project.
Unless mentioned otherwise, the data acquisition parameters used for data acquisition and data processing of the EMG signals are presented in table 5.1. Further explanation regarding each of the parameters will be presented in the dedicated subsections.
Information regarding the bandwidth of EMG signals varies between literature being that the entire bandwidth can be from 0 Hz to anywhere between 400 to 500 Hz ([20]–[22]). In this project, the sampling frequency (f_s) matches the one from [21], which was 1250Hz. The Nyquist theorem states that, in order to obtain a proper reconstruction of a signal, the sampling frequency has to be at least twice the maximum frequency of the signal. With this information, and considering a maximal frequency of 500 Hz for a given EMG signal, this sampling frequency is enough to get an accurate reconstruction of the signal.

5.3 Filtering

The EMG signal power spectrum is spread over a large range of frequencies, yet not all of them possess relevant information. Furthermore, due to the acquisition process itself, there are components of the signal that are not only signal but carry with it noise. The noise can come from a variety of sources, depending on whether the subject moves during the recording, amongst other things. This means that after the recording of the signal there is a need

Parameter		Description	Section
Sampling Frequency (fs)		1250 Hz	5.2
Window Size		200 ms	5.4
Overlapping		50%	5.4
Cutoff Frequency	Lower Bound	5 Hz	5.3
	Upper Bound	450 Hz	
Filter Used		Direct-form II filter	5.3

Table 5.1: List of parameters used to acquire and process EMG data.

to filter the signal so that predominantly relevant information remains.

In order to choose the proper filter to use, it is necessary to look at the properties of the signal. Since the data is only composed of discrete samples, it is necessary to implement a digital filter. There are two main types of digital filters - finite impulse response (FIR) filters, and infinite impulse response (IIR) filters. Moreover, given the future specifications of the project, that is, the need for the entire system to work online, there is automatically the need to implement a causal filter. The main difference between FIR and IIR filters is that the first take only a limited number of past input samples, while IIR filters produce an output based on a weighted sum of all past samples and the current input. There are a couple of disadvantages of using IIR filters, particularly, they do not have a constant phase and they can become unstable. Despite this fact and the low computational effort that these require, in comparison to FIR-type filters, these were the ones selected to be implemented. Regarding the method of implementation, there are two direct-forms for the implementation of an IIR filter. Direct-form-II is canonical with respect to delay, because two poles and two zero sections of the filter transfer function are shared, making the delay of the filter constant across the board. This generates less variance in a real life situation and creates stability in the code implementation.

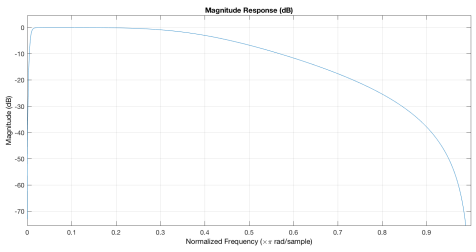

Figure 5.2: Frequency response of the chosen digital filter

Overall, most literature recommends to apply a high pass filter to the EMG signals in the

range of 50 Hz (in European countries), since it is easier to see, in the power spectrum of the acquired signal, a value of this frequency corresponding to the power provided by the mains. [22]. On the other hand, the Refa equipment utilises a floating measurement system that avoids this problem, using a fifth order bandpass filter with a lower cutoff frequency of 5Hz and upper cutoff frequency of 450 Hz for the filtering of the EMG signal. The upper cutoff frequency was determined, since overall literature presents as an acceptable value anything between 400 and 500 Hz [23].
The code used for this section of the project was implemented in MatLab, and the filter chosen was created by the function *dfilt.df2*, which takes as input the coefficients of the numerator and denominator of that establish the transfer function of the filter. These were created by the function *butter*.

5.4 Data Segmentation

As previously mentioned, data was acquired using a Refa amplifier (TMSi, Oldenzaal, NL), which is a device with a sampling frequency of 1250 Hz. This means that at each second of recording there are $N \times 1250$ samples of data available, where N is the number of electrodes. Too many samples can create problems; first, it makes it harder later on in the classification procedure to distinguish between different sets of movements (less accuracy); second, it takes longer to process the data. This being said, the goal of data segmentation is to apply techniques to process in order to prepare the data for subsequent extraction and make the entire process more time efficient (greater response time).
A segment is comprised of a short data sequence (or fragment) limited by a time frame which is used to determine signal features. The length of this segment needs to be a compromise between the response time and the accuracy. Too short of a window can lead to bias and variance, on the other hand, too long of a window can lead to the loss of critical information, hindering future endeavours due to the loss of critical information. It has been found ([24]) that epoch lengths smaller than 125 ms are to be avoided for stationary signals. This being said, longer windows bring larger levels of delay in online classification. It was found ([8], [25]) that for a window length of 200 ms the delay would be of 1.1 ms with a system that matches the characteristics of the one used to perform the tests presented in this report. This value is negligible in real-time, as such, this was the epoch length used in this project. Furthermore, it was established as well that overlapping does not bring any additional value for electromyography processing whilst only increasing computational time [26].

5.5 Classification

The study of Pi-ETPU based electrodes should not only revolutionise the electrode industry, but it should also be the innovation that intends to solve most of the problems associated with prosthetics. That is, lowering the cost of one of the still limiting factors, which is the price of the electrodes that incorporate said prostheses.
This work falls in line with the SoftPro project, which looks into innovative and out of the box solutions for the development of ”new prostheses, exoskeletons, and assistive devices for upper limb rehabilitation” [27]. As previously mentioned, the idea behind machine learning is the development of algorithms that are able to predict outcomes based on behaviours or patterns. If these patterns can be established from EMG readings, and if this classifier is connected to a controller which can be connected to a robotic arm, then there is the possibility of virtually controlling a robotic arm.
Regarding myoelectric control, there are two types of classifiers that were approached in this project. Due to the relative low computational effort of Linear Discriminant Analysis (LDA), this was one of the first classifiers that was implemented in the project. However, Support Vector Machine (SVM) is more precise and provides better results, but its cost of computational effort is higher.

5.5.1 Linear Discriminant Analysis Classifier (LDA)

Linear Discriminant Analysis is a type of pattern recognition algorithm which does not require a lot of computational effort and is still able to achieve very good results. Its goal is to maximise the separability between classes by projecting them into a lower dimensional space.
The following explanation will be based on a book by Bishop [28] and on [29].

Assumptions

In order to split the data into a lower dimensionality space, LDA makes a number of assumptions. By performing the following, LDA skips a series of normality as well as other types of mathematical checks in order to split the data.

- Data is normally distributed
- Features are statistically independent
- Identical covariance matrix for every class

The dimensionality reduction goals of LDA are accomplished by the creation of a new axis that maximises the separability between classes. The position of this new graph is determined in such a way that the mean (μ) between classes is maximised and the scatter (S) of each class is minimised.

As a reference, it is possible to imagine the red dots in Figure 5.3 as being of class C_1 and the green dots as from another class C_2. The means of both classes are presented in equation 5.1, where N_1 and N_2 are, respectively, the number of samples in class C_1a nd C_2.

$$\mu_k = \frac{1}{N_k} \sum_{i \in C_k} x_i \tag{5.1}$$

$$\begin{bmatrix} \mu_1 \\ \mu_2 \\ \vdots \end{bmatrix} = \begin{bmatrix} \frac{1}{N_1} \sum_{i \in C_1}^{N_1} x_i \\ \frac{1}{N_2} \sum_{i \in C_2}^{N_2} x_i \\ \vdots \end{bmatrix}$$

Equation 5.2 defines the scatter within the class. In a two-class example, the equation can be simplified into equation 5.3.

$$\begin{aligned} S_w &= \sum_{i \in C_i}^{C} S_i \\ S_i &= \sum_{i \in C_i}^{n} (x - \mu_i)(x - \mu_i)^T \end{aligned} \tag{5.2}$$

$$S_w = \sum_{i \in C_1} (x_i - \mu_1)(x_i - \mu_1)^T + \sum_{i \in C_2} (x_i - \mu_2)(x_i - \mu_2)^T \longrightarrow \text{For a two class case} \tag{5.3}$$

Furthermore, the scatter between the classes needs to be calculated, and that is presented in equation 5.4.

$$\begin{aligned} S_b &= \sum_{i=1}^{C} (\mu_i - \mu)(\mu_i - \mu)^T \\ S_b &= (\mu_2 - \mu_1)(\mu_2 - \mu_1) \longrightarrow \text{For a two class case} \end{aligned} \tag{5.4}$$

Returning to the maximisation problem, Fisher's proposal is to draw the new hyperplane in a way that maximises the separability of the means of both classes and minimises the scatter. If there are eigenvectors v that satisfy the condition $S_w^{-1} S_B v = \lambda v$, then v provides information regarding the transformation of the original hyperplane into a new one, and λ provides information regarding the strength of such a transformation. The last step is doing the transformation of the points from the old hyperplane to the new and reduced one. The

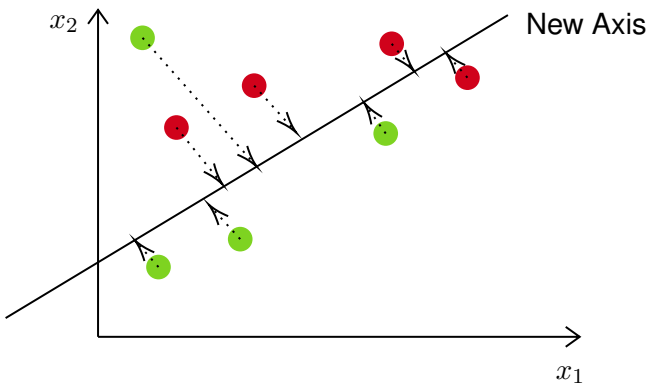

Figure 5.3: Scheme1

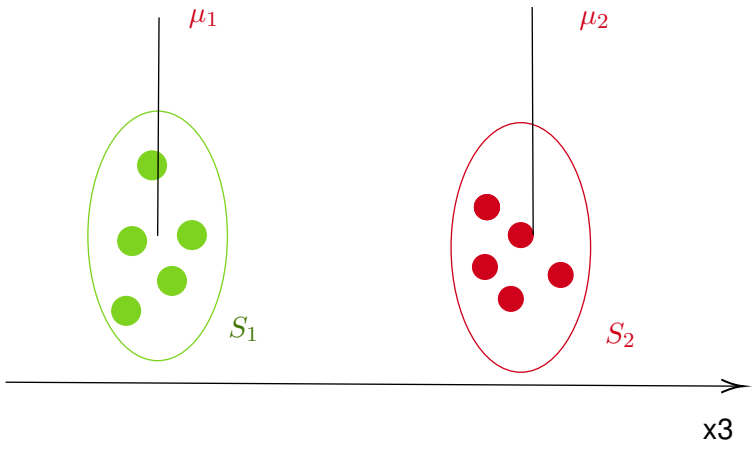

Figure 5.4: Scheme2

separation of the data in a new plane allows to set threshold values in order to make a separation between classes.
The following explanation presents the simplified reasoning of LDA for a two dimensional situation as seen in figures 5.3 and 5.4. In the current project being developed, the concept is more complicated but still valid. In this case, the red and green points will be defined originally in a 8-coordinate system, depending on the number of electrodes that constitute the armband. The classes will not be only red and green, but there will be 3 or 5 according to the amount of movements (classes) being used. The difference in the new situation is that the goal is to maximise the distance between the mean of each class and a central point between all classes. In this project, LDA was implemented using Matlab's function *fitcdiscr*.

5.5.2 Support Vector Machine (SVM)

Support Vector Machine (SVM) has risen in popularity due to its ability to achieve high performance in complex models. They have been used for a wide range of applications, including pattern recognition using myoelectric signals ([30], [31]). In the present section, the fundamental concept of SVM will be presented based on [28] and on Vapnik's original publication [12].

The simplest case possible is comprised of a binary classification, presented by the positive and negative examples, and the goal is to draw a straight line with the view towards generating the maximum separation between the positive examples and negative examples. In order to do this, it is necessary to create a decision rule that would use that decision boundary. To do that, we take $\vec{\omega}$ with variable length but perpendicular to the media line of the street. Furthermore, we have $\vec{u}$ which is a given unknown that can lie anywhere in the plane. The goal is to make a projection of $\vec{u}$ in $\vec{\omega}$ in such a way that the norm of that projection will give information whether the sample lies in the left side of the street or the right side of the street (this formulation is given by the decision rule presented in equation 5.5, where b is an arbitrary, bias variable).

$$\vec{\omega} \cdot \vec{u} + b \geq 0 \tag{5.5}$$

The solution to this problem lies in the setting of additional constraints in order to make it possible to calculate b and $\vec{\omega}$. Those contraints are first expressed in equation 5.6 where it is presented that, for a given positive sample, the solution of 5.5 will be greater or equal

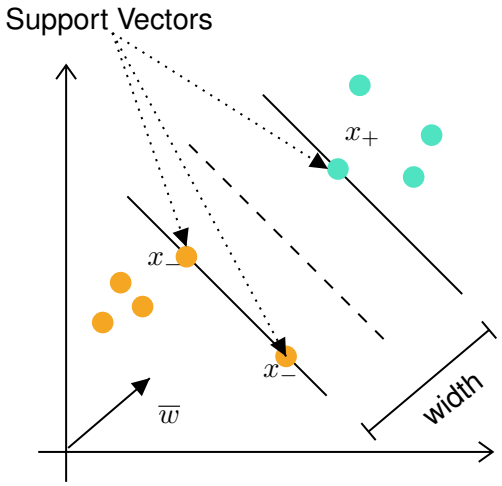

Figure 5.5: Representation for the separation of a binary class using SVM

.

than 1 for a positive sample, and smaller or equal to -1 for a negative sample.

$$\begin{aligned} \vec{\omega} \cdot \vec{u}_+ + b \geq 1 \\ \vec{\omega} \cdot \vec{u}_- + b \leq -1 \end{aligned} \tag{5.6}$$

For mathematical simplification, a new variable y_i is introduced so much so that $y_i = +1$ for positive samples and $y_i = -1$ for negative samples. By multiplying each of the equations of 5.6 by y_i, then both equations are simplified into one single equation given by 5.7.

$$\begin{aligned} y_i(\vec{x}_i \cdot \vec{\omega} + b) \geq 1 \\ y_i(\vec{x}_i \cdot \vec{\omega} + b) - 1 \geq 0 \end{aligned} \tag{5.7}$$

Do not forget that the main question in this problem is to maximise the distance between the lines and the width of the margins, which can be expressed by equation 5.8. Because we are setting the problem in a way that x_+ and x_- are in the borders, from equation 5.7 the value of $\vec{x}_+ \cdot \vec{\omega}$ and $\vec{x}_- \cdot \vec{\omega}$ will be 1-b and 1+b respectivelly. The result is the simplification given in equation 5.8 (for detailed information check Appendix A.1).

$$\begin{aligned} W = (\vec{x}_+ - \vec{x}_-) \cdot \frac{\vec{\omega}}{||\vec{\omega}||} \\ W = \frac{2}{||\vec{\omega}||} \end{aligned} \tag{5.8}$$

The problem remains argmax $\left(\frac{2}{||\vec{\omega}||}\right)$, which is the equivalent to look for argmin $\left(\frac{1}{2}||\vec{\omega}||^2\right)$. In order to solve this equation, constrained by equation 5.7, we should search for the minimum of a function that is constrained. In order to solve this problem, it is possible to apply Lagrange multipliers. This is expressed by equation 5.9, in which L is the function that we

intend to minimise. The first argument of the expression comes from equation 5.8, and the second term of the expression is the addition of all the constraints multiplied by an arbitrary parameter α_i.

$$L = \frac{1}{2}||\vec{\omega}||^2 - \sum_{i=1}^{N} \alpha_i [y_i(\vec{\omega} \cdot \vec{x}_i + b) - 1] \tag{5.9}$$

In order to find the minimum (and maximum) of equation 5.9, it is necessary to take the partial derivatives of L and set them to zero. By doing so, the expressions presented in equations 5.10 and 5.11 are obtained. Please note that the most interesting part of this is that the decision vector $\vec{\omega}$ is a linear sum of the samples $\vec{x}_i$.

$$\begin{aligned} \frac{\partial L}{\partial \vec{\omega}} &= \vec{\omega} - \sum_{i=1}^{N} \alpha_i y_i \vec{x}_i = 0 \\ \vec{\omega} &= \sum_{i=1}^{N} \alpha_i y_i \vec{x}_i \end{aligned} \tag{5.10}$$

$$\frac{\partial L}{\partial b} = -\sum_{i=1}^{N} \alpha_i y_i = 0 \implies \sum_{i=1}^{N} \alpha_i y_i = 0 \tag{5.11}$$

In order to find the minimum of the equation 5.9, the next step is to input equation 5.10 into 5.9, from which it is possible to see equation 5.12. This also means that the optimization of the function only depends on the pairs of $\vec{x}_i \cdot \vec{x}_j$.

$$L = \sum_{i}^{N} \alpha_i - \sum_{i=1}^{N} \sum_{j=1}^{N} \alpha_i \alpha_j y_i y_j \vec{x}_i \cdot \vec{x}_j \tag{5.12}$$

It is important to note that this optimisation procedure does not stay stuck at a local maxima due to the fact that this is a convex space. This means that SVM presents concrete advantages to algorithms like neural networks that easily get stuck in local maximals. The problem of this algorithm lies when the classes are not linearly inseparable, then the solution lies in switching perspectives, that is, to do a projection into another space. Furthermore, given that the maximisation of L only depends on the dot product between two vectors, the projection into another space only requires to be made via the dot product in between two vectors. This means that it is necessary to maximize $\phi(\vec{x}_i) \cdot \phi(\vec{x}_j)$, where $\phi(\vec{x}_i)$ is the transformation of vector $\vec{x}_i$ into another space, and $\phi(\vec{x}_j)$ is the transformation of $\vec{x}_j$ into another space. Furthermore, from the decision rule, in order to recognize whether the variable is positive or negative, all that is necessary is the decision rule function $\phi(\vec{x}_i) \cdot \phi(\vec{u}) >= 0$
Moreover, if I have a function K, as represented by equation 5.13, it is not necessary to

know the transformation of those two vectors into another space, since the value of said function returns the dot product of both vectors.

$$K(x_i, x_j) = \phi(\vec{x}_i) \cdot \phi(\vec{x}_j) \tag{5.13}$$

In this project in particular, the SVM system is built in MatLab making use of the function *fitcecoc* with the option Hyperparameter Optimization set to the *all* option. This means that the function will optimise the fitting of the data using all three kernels MatLab has available, which are the Gaussian, the linear and the polynomial kernels. Their functions are respectively presented in equations 5.14 - 5.16.

$$K(x_i, x_k) = \exp^{-||x_i - x_j||^2} \tag{5.14}$$

$$K(x_i, x_k) = \vec{x}_i \cdot \vec{x}_j \tag{5.15}$$

$$K(x_i, x_k) = (\vec{x}_i \cdot \vec{x}_j + 1)^n \tag{5.16}$$

5.6 Methodology

Two structures, identical to the one presented in Figure 4.1, were printed in order to perform the systematic evaluation. Two of the structures in Figure 5.6 were printed to perform the functional evaluation. Each strip is composed of four electrodes, and both combined compromise a 8-electrode armband. The printing specifications of both structures were the same as the ones presented in Table 4.1. Following the signal acquisition pipeline approach in the previous sections of this chapter, the goal of the following methodology is to establish a comparison between the signal acquired from a set of AgCl electrodes and the Pi-ETPU electrodes.

Functional Evaluation

The functional evaluation of the printed electrodes will be based on the classification accuracy. As mentioned in the beginning of this chapter, commonly used classifiers for EMG applications are LDA. The following procedure will be repeated twice, once for the AgCl

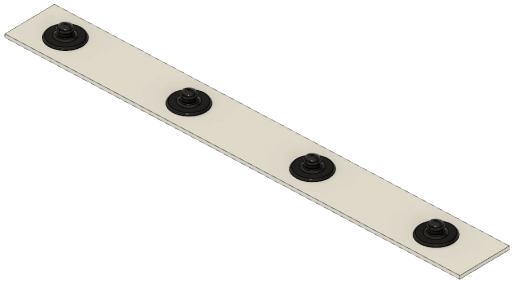

Figure 5.6: Printed Structure (4 Electrodes)

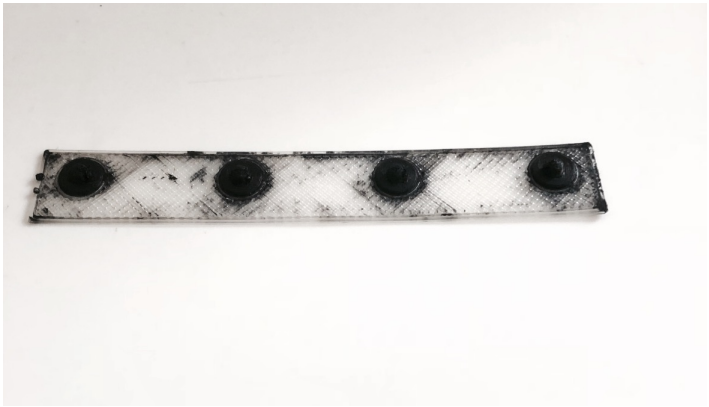

Figure 5.7: Printed half of the armband.

electrodes and once for the Pi-ETPU electrodes. The subject was placed in a comfortable position, either sat down or up straight, but with the notion that he should perform all the movement training with the arm in the same position. The skin was prepped with Gel-Prep (Nuprep, USA), the excess was cleaned with a cloth and the skin was then rubbed with alcohol. This process, which is the same as the systematic evaluation of the electrodes, has to do with the removal of dead skin in order to improve the contact of the electrode with the skin. The 8-electrode armband was placed on the right arm below the elbow, and fixed with Leukofix, it was found that this method allowed for closer contact of the electrodes with the skin by maintaining the armband tighter.
Each electrode was connected to the Refa, and the ground of the device, consisting of a damp cloth with a snap button connection, was placed on the opposite arm to which the armband was attached.
The recording of signals (for the training of the classifier) goes as follows:

- **Rest Recording**. During 9 seconds, the subject stood still and the rest EMG recording was performed.

- **Recordings of each class**: The following Process was repeated for each class.

  - Recording of maximum voluntary contraction (MVC) of that movement: 9 second recording with 3 seconds of rest and 6 seconds of full contraction. The goal of this is to gather the MVC. The value is calculated as follows. From the entire 6 seconds of contraction I retrieve the maximum recorded value from each electrode. The MVC value is the norm of this vector.
  - 9 seconds recording consisting of 3 seconds of rest followed of 6 seconds of contraction at 30% MVC. The percentage of MVC is calculated as follows. The maximum electrode value of each electrode from the past 5 window segments is stored in the vector, and the norm of said vector is calculated. The percentage is the quotient between the norm of this vector and the MVC value for the movement that is being done times 100.
  - 9 seconds recording consisting of 3 seconds of rest followed of 6 seconds of contraction at 50% MVC.
  - 9 seconds recording consisting of 3 seconds of rest followed of 6 seconds of contraction at 70% MVC.

- **Offline generation of the classifier** When the training procedure is finished the LDA and SVM classifiers were built by using Matlab's *fitcdiscr* and *fitcecoc* respectively. After the classifiers are built, 10 fold cross validations using the training data is used in order to obtain the confusion matrixes presented in section 5.7. The confusion matrix is obtained using Matlab function *plotconfusion*.

- **Online testing of the classifier**: The online testing follows exactly the same pipeline as before but now while the subject is performing movements the classifier is producing outputs.

Systematic Evaluation

Allied to the classification performance of both electrode bands, it is relevant to also compare the power distribution of the signals over the frequency band in order to see if they are comparable.
Furthermore, the signal-to-noise ratio (SNR) of the electrodes was calculated. The formula used to determine the SNR value is present in Equation 5.17, where the power of the signal is the power of the signal acquired when contracting and the power of the power of the noise is the power of the signal when not contracting.

$$\text{SNR (dB)} = 20 \times \log(\frac{P_{\text{Signal}}}{P_{\text{Signal}}}) \tag{5.17}$$

Figure 5.8: Class 0

Figure 5.9: Class 1

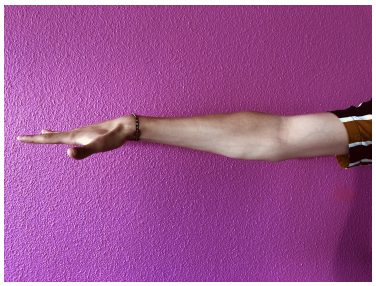

Figure 5.10: Class 2

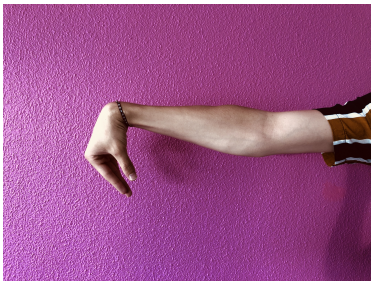

Figure 5.11: Class 3

Figure 5.12: Class 4

Figure 5.13: Class 5

5.7 Results

Functional Evaluation

Table 5.2 presents a summary of the classification results using both types of electrodes. Naturally, there is a decrease in classification when incrementing the number of classes, but overall the results are very good. Notably, the results provided from the Pi-ETPU-based electrodes are even better than the AgCl electrodes, and the loss of accuracy, with the increment of classes particularly with the SVM classifier, is lower than the silver chloride ones. In more detail, it is possible to look at Figures 5.14 and 5.15, where the confusion matrix for the SVM classifier of both electrodes is present. As it is possible to see, class 5 (pinch motion) presented the best accuracy for the AgCl electrodes, while class two had the best accuracy for the Pi-ETPU electrodes.

The functional evaluation is focused in the confusion matrix provided by the training procedure. The confusion matrix is acquired via the Matlab function *plotconfusion*. The ”target

class", corresponds to the true movement class, and the "Output Class" represent the classification provided by the classifier. Therefore, looking into the confusion matrix it is possible to see that the diagonal are the correctly classified classes while the other ones are misclassified. The bottom row presents the true positive rate and false negative rate associated with each class. More specifically, looking at one column in particular, it is possible to gather the percentage of times that the classifier correctly classified the movement. The columns on the far right of the confusion matrix presents the accuracy, that is, if focus is given in one row, it is possible to see of all the times that the classifier outputted that given class, the percentage of times that it was in fact correct. Last but not least, in the bottom tight of the confusion matrix it is possible to gather the overall accuracy of the classifier. This is the value presented the tables that will follow in the results and discussion section of this chapter. Overall from the results provided by the confusion matrix it is possible to gather information regarding what classes are being the worst classified and with which are they being misclassified with.

Classifier		AgCl	Pi-ETPU
LDA	3 Class	85.5 %	88.6%
	5 Class	81.6%	86.5%
SVM	3 Class	90.4%	90.9%
	5 Class	86.8%	90.6%

Table 5.2: Classification accuracy of each classifier

Systematic Evaluation

Figure 5.16 present the signal gathered for a fist flexion contraction using the AgCL and Pi-ETPU Electrodes. Figures 5.17 to 5.20 present the splitting of data into rest and contraction from figure 5.16 in order to calculate the SNR values of each electrode. The results have returned a SNR value of 45.75 dB for the AgCl electrodes and 14.48 dB for the Pi-ETPU 700+ based electrodes.

Figures 5.21 to 5.28, present the power distribution of each electrode of the armband for the AgCl electrodes and the Pi-ETPU electrodes. As it is possible to see, from the power distribution of all electrodes, the signal acquired with the Pi-ETPU is similar to the AgCl Electrodes.

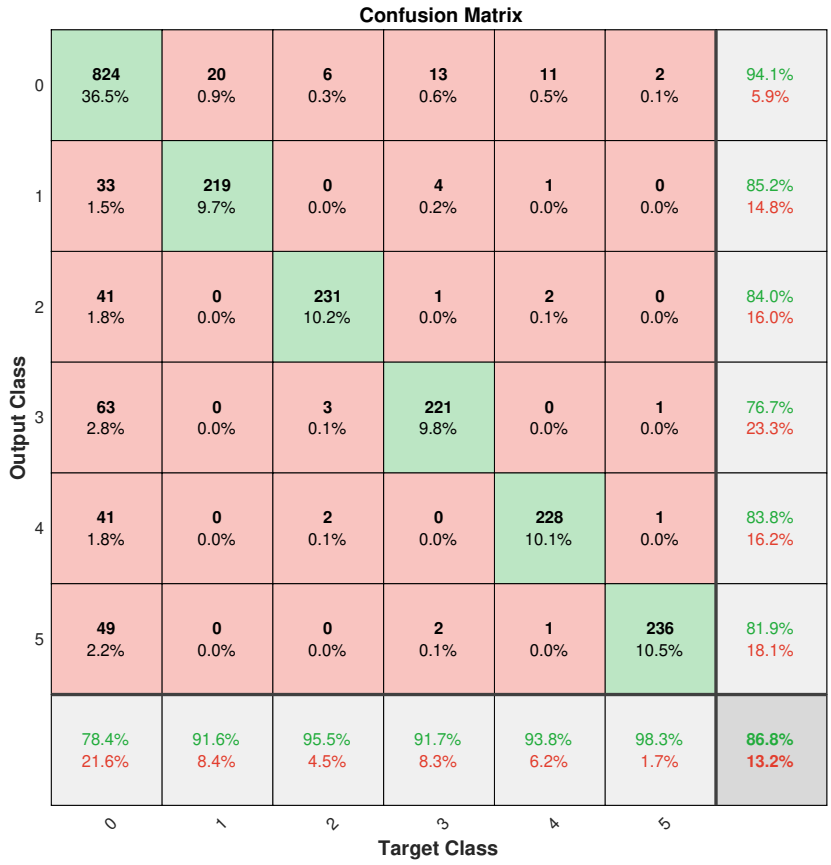

Figure 5.14: SVM 5 class AgCL

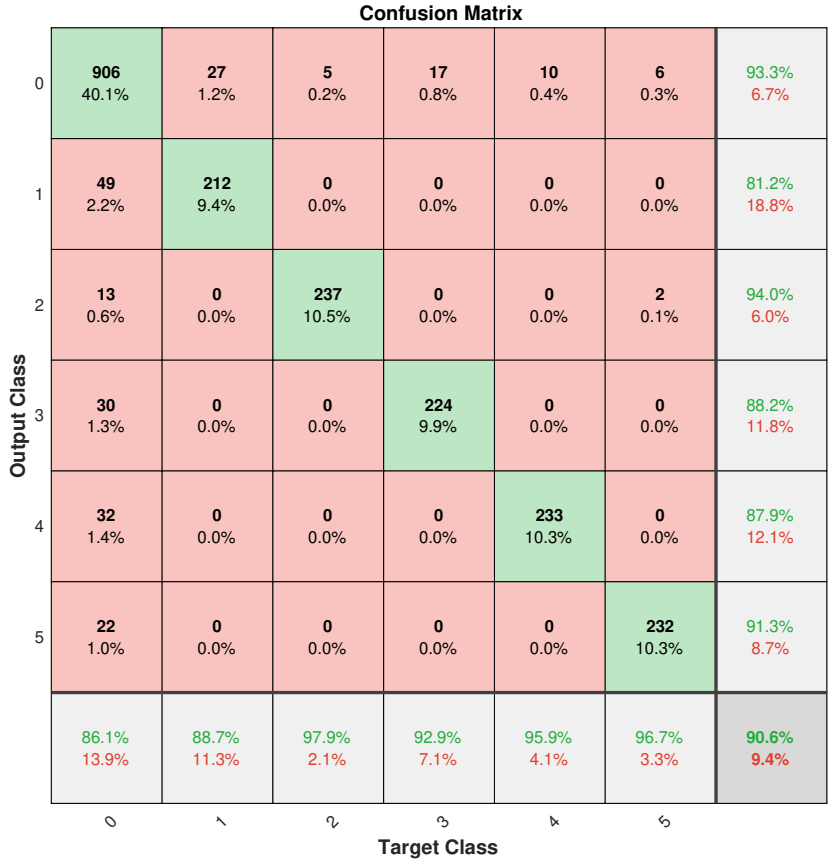

Figure 5.15: SVM 5 class Pi-ETPU

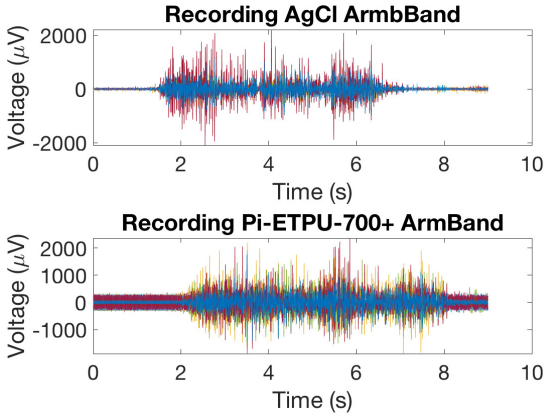

Figure 5.16: Fist flexion contraction using AgCL and Pi-ETPU Electrodes

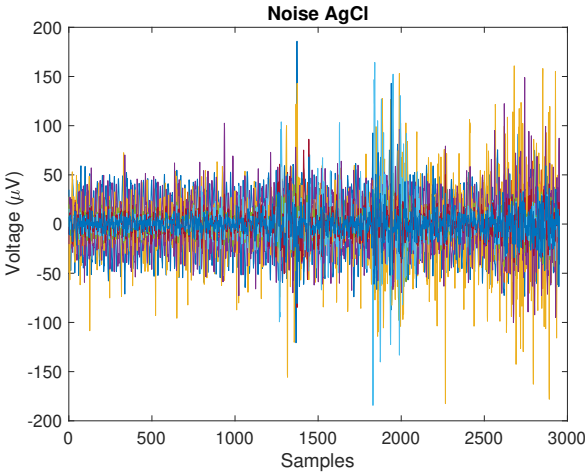

Figure 5.17: Noise AgCl

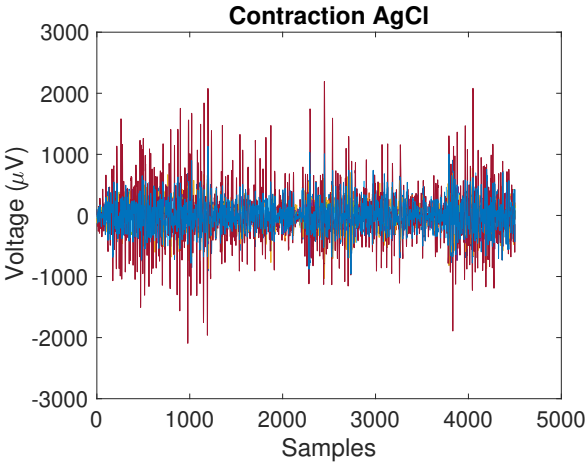

Figure 5.18: Contraction AgCl

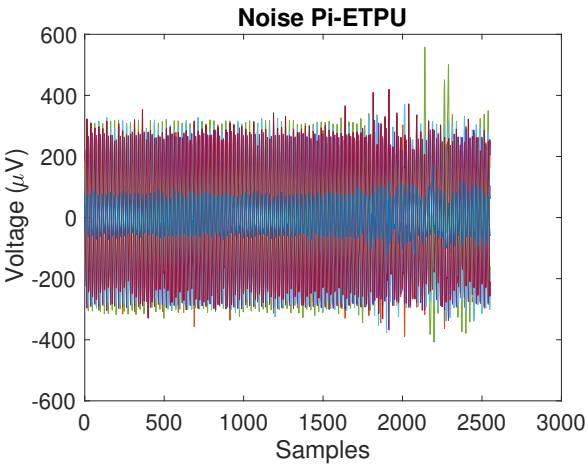

Figure 5.19: Noise TPU

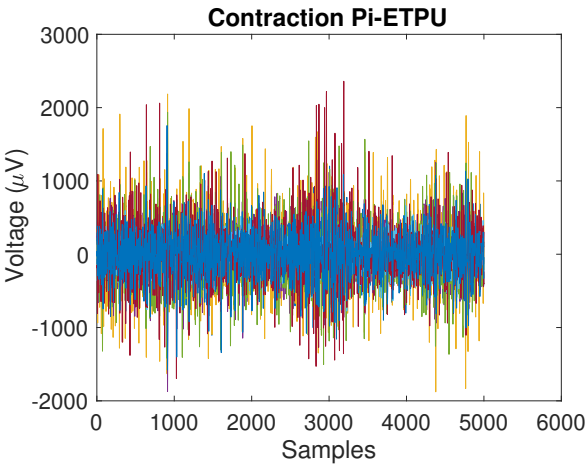

Figure 5.20: Contraction TPU

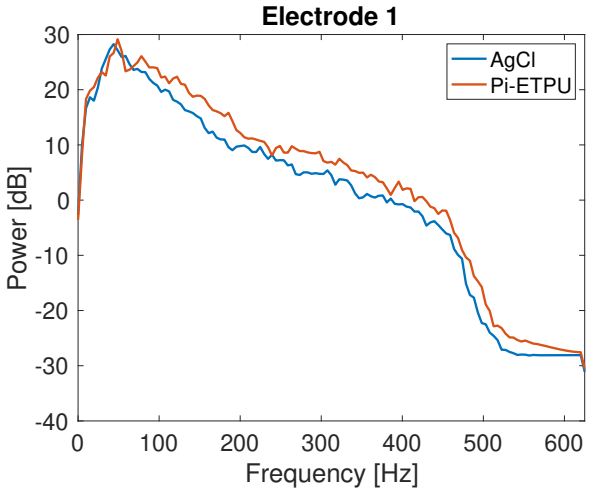

Figure 5.21: PSD Electrode 1

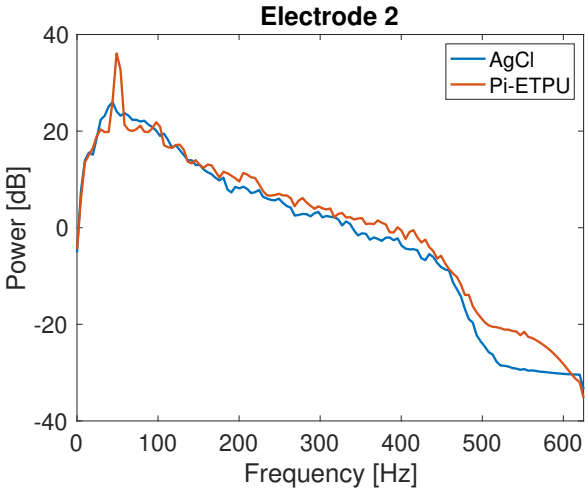

Figure 5.22: PSD Electrode 2

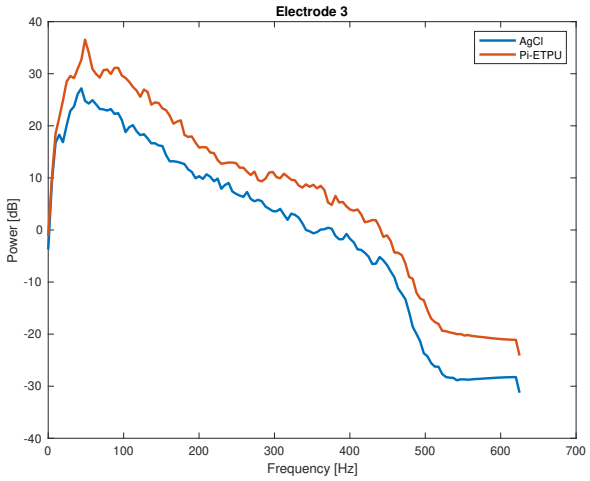

Figure 5.23: PSD Electrode 3

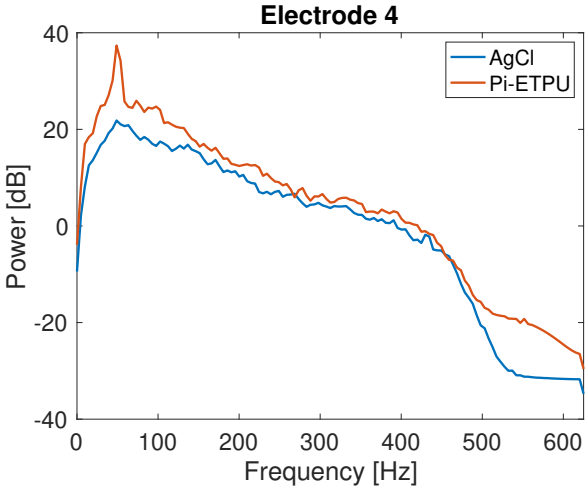

Figure 5.24: PSD Electrode 4

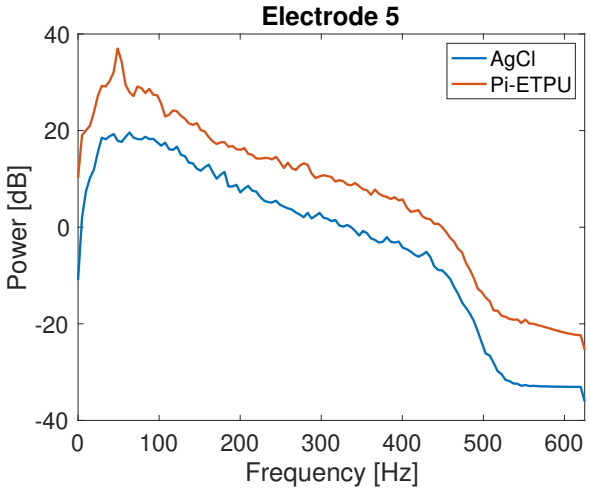

Figure 5.25: PSD Electrode 5

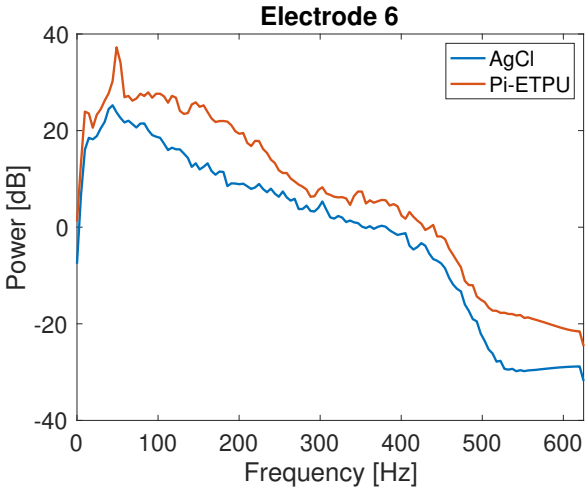

Figure 5.26: PSD Electrode 6

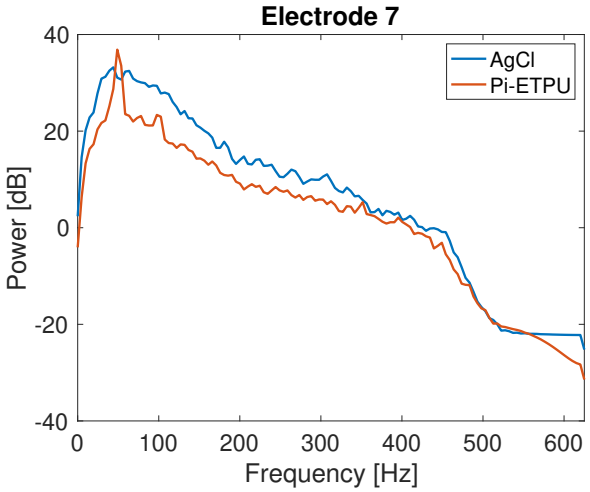

Figure 5.27: PSD Electrode 7

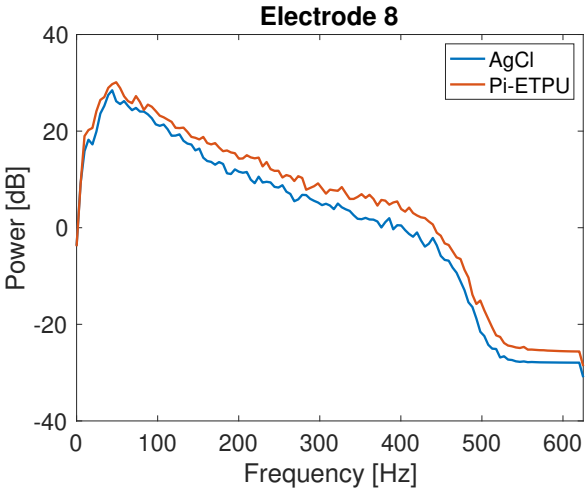

Figure 5.28: PSD Electrode 8

5.8 Discussion

First, regarding the systematic evaluation of the electrodes, it is possible to see that the power distribution of the electrodes for AgCL and Pi-ETPU are similar, and similar to what is seen overall in the literature ([32], [11]). Furthermore, it is possible to verify that the SNR ratio for the Pi-ETPU based electrodes, is significantly lower than of the AgCl ones. These values are consistent to what is seen in the results provided by figures 5.17 and 5.19. From the previous chapter, it was possible to gather that the contact resistance of the Pi-ETPU electrodes was significantly higher than the AgCl ones. Its is fare to assume that this increment in contact resistance is affecting the SNR value of the recording.

Regarding the functional evaluation of an 8-electrode armband, the Pi-ETPU-based armband classification has surpassed the results provided by the gold standard electrodes. The results have shown that most of the classification error comes from the misclassification of movements in rest. Notably, this is expected, since no post-processing was applied to the classifier after the cross validation procedure. Applying majority voting, for example, would smoothen the output of the classifier and improve these types of errors.

Moreover, looking at the power distribution of the electrodes, it is possible to see that the power distribution of the Pi-ETPU and the AgCL electrodes are comparable, they follow the same slope and they have approximately the same distribution. What is more noticeable is the 50Hz peak of the Pi-ETPU electrodes that comes from the mains. This can be explained for the fact that the Pi-ETPU electrodes have a much higher impedance than the solver chloride ones and, as of such, the OpAmps systems inside the Refa is no longer able to compensate for this factor as it is in the AgCl.

Overall, the classification results of the Pi-ETPU electrodes has surpassed the gold-standard. Despite the worse SNR value that electrodes have shown, there is still a lot of signal processing that is placed. The results have shown the despite the physical limitations of the electrodes, all the pos-processing of the signals is able to override this limitation and still provide with better classification accuracy. Given the high optimal accuracy of the results presented in this chapter, another discussion that arises is how increasing the number of electrodes and changing their size could affect the overall performance of the classifier. The reason behind these questions lies not only in the goal of reaching a 100 % accuracy during classification, but in the aesthetic appearance of the armband.

5.9 Conclusion

The classification results have proven the ability of an 8-electrode armband to distinguish between discrete movements but, as it is natural, the values obtained in this chapter are too dependent on the quality of the training, and how familiarised the user is with the it. Additionally, the dataset gathered from one patient is not enough to build a classifier that can be generalised for industry applications. As it was discussed in Chapter 2, even off the shelf products for upper limb prostheses still require a period of adaptation an training. This has to do with a variety of factors such as the sensitivity of the classifiers to the positions of the electrodes as just by removing and putting again the electrodes in the arm will decrease the performance of the classifier. This situation is worsened when using the same classifier in different subjects, not only because of the movement of the electrodes in relation to the muscle, but also due to the variation of parameter such as arm size, degree of hairs and even the layers of fat present in the skin.

Chapter 6

Shape and Density Analysis

6.1 Introduction

In the previous chapter, the reliability of Pi-ETPU-based electrodes was proven for the classification of up to five discrete movements. In order to investigate on how the classification accuracy would be affected by different sets of different-sized electrodes and different electrode density, the following methodology was set in place.

6.2 Electrode Density

6.2.1 High Density EMG

In the last couple of years, a lot of focus has been concentrated on high density EMG grids. These grid systems, in theory, allow the precise identification of the activity of single motor units [33] and are composed of a large number of small electrodes. With the development of research and science, these technologies have come to the field of prosthetics, and studies have been made with rather positive results regarding the classification of movements ([34], [35]) like this research has presented until this point.
By looking at examples like this, one of the options would be to increment the number of electrodes and the reduction of their size, in order to improve the classification performance using the originally designed armband. Originally, the armband was composed of 8 electrodes, the minimum required by the guidelines, in order to have a viable level of classification. Given that the equipment available had the possibility to go up to 16-channels, it was decided to increment the number of electrodes up to 16.

6.2.2 Methodology

Electrode Size

The first stage of incrementing the level of electrode density consisted of reducing the electrode size from 10 mm in diameter to 5 mm in diameter. Figure 6.1 presents the scheme of the designed armband for this study.

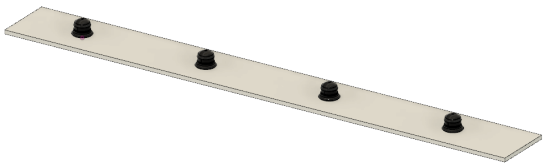

Figure 6.1: Structure will smaller electrodes

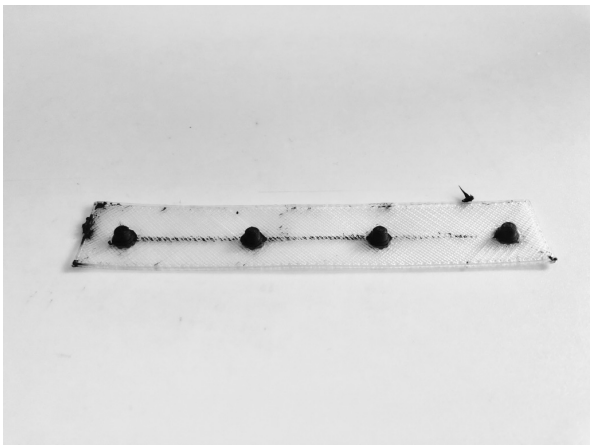

Figure 6.2: Photo of the structure with smaller electrodes

Electrode Density

Figure 6.4 shows the designed strip of electrodes which, compared to the original one, has twice the number of electrodes in the same length.

For both structures, the full armband used in the subject was composed of two of each of these structures. All structures were printed according to the specifications of table 4.1, but with different size. When printing the armband with smaller electrodes, the electrodes have a size of 5mm, whilst the high density armband remains with an electrode diameter of 10 mm.The data acquisition methodology and the movements performed were exactly the same as the ones presented in Chapter 5 and performed by the same subject as before.

Figure 6.3: Structure with higher density of electrodes

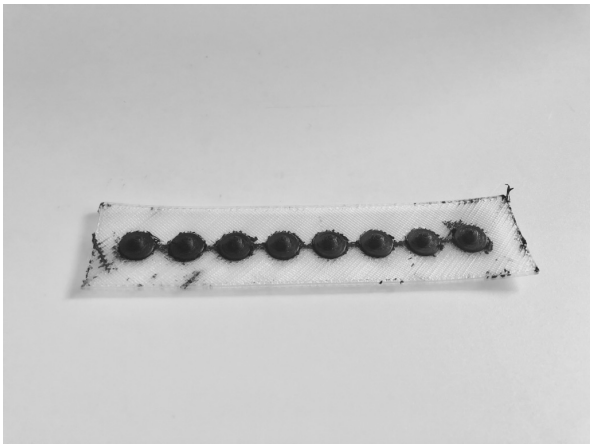

Figure 6.4: Photo of the structure with more electrodes

6.2.3 Results

Table 6.1 summaries the classification results with the two new structures in comparison to the one studied in the previous chapter. As it is possible to see for 5 classes using an LDA classifier, the classification dropped 8.2% and 14.3%, respectively, for the structure with smaller electrodes and for the structure with higher amount of electrodes. For the SVM, the drop was less sharp for the first structure 6.9%. On the other hand, it worsened for the high density structure with a drop in 16.3%.

Figures 6.5 and 6.6 present the confusion matrixes for both structures using the SVM classifier, and the results are very much similar between them and for the confusion matrix of the previous chapter. Rest remains a movement that continues to be misclassified frequently. In the high density armband, palm extension (class 2) presented a worse than normal classification accuracy, being frequently misclassified as wrist flexion (class 4) or rest (class 0). In reality, this result makes sense since both these movements use the flexor muscles in the lower part of the lower arm.

Classifier		8 Electrodes	8 (Small) Electrodes	16 Electrodes
LDA	3 Class	88.6%	86.4%	79.5%
	5 Class	86.5%	78.3%	72.2%
SVM	3 Class	90.9%	86.9%	82.7%
	5 Class	90.6%	83.7%	74.3%

Table 6.1: Classification Performance Table

6.2.4 Discussion and Conclusion

One of the major results provided by the previous ones show a large drop in classification using a high density armband. Contrary to the idea that ”more is better”, clearly a high density of electrodes is not better in this case. In order to try to understand why the classification dropped, some time was devoted to study the data gathered during the recording. First, cross correlation between the signals acquired during the recording was performed. Given that there were 16 electrodes, this returns 137 correlations between signals of electrodes. After performing this, the results became quite inconclusive, as comparing the signals from different electrodes lead to a very high correlation. The goal of correlating signals would be to see if two electrodes, which would be very close to each other, would read the same signals. If this would be proved, then the cross talk between electrodes could be proved, which in turn would mean that, by adding electrodes to the only practical thing that was being done, this was adding more information, but not adding more relevant information.

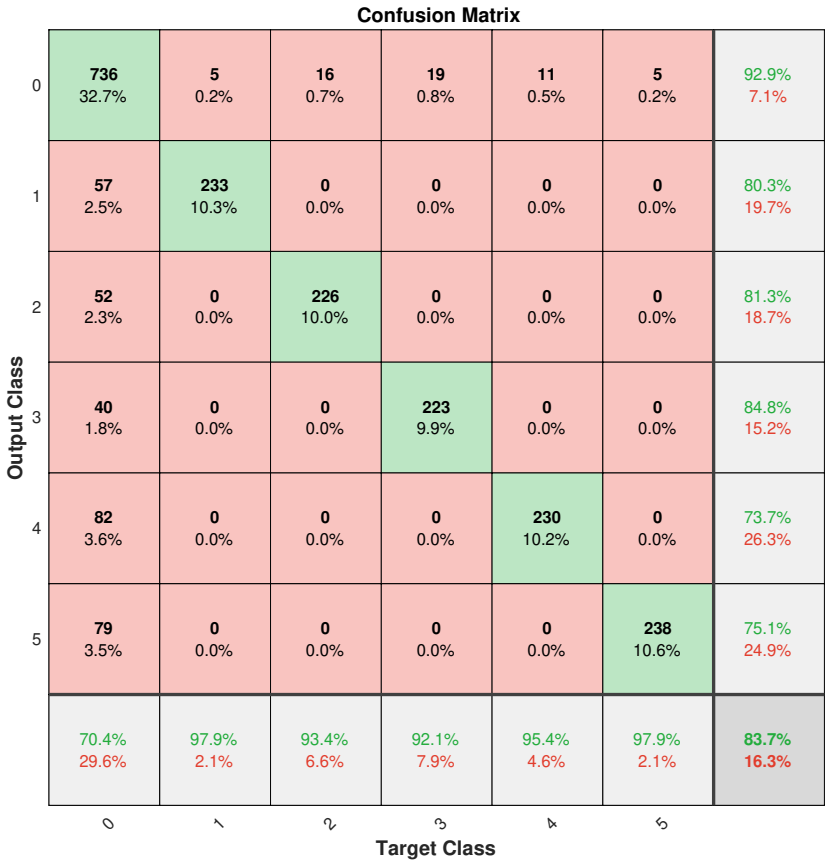

Figure 6.5: CM, 8 (Small) Electrodes

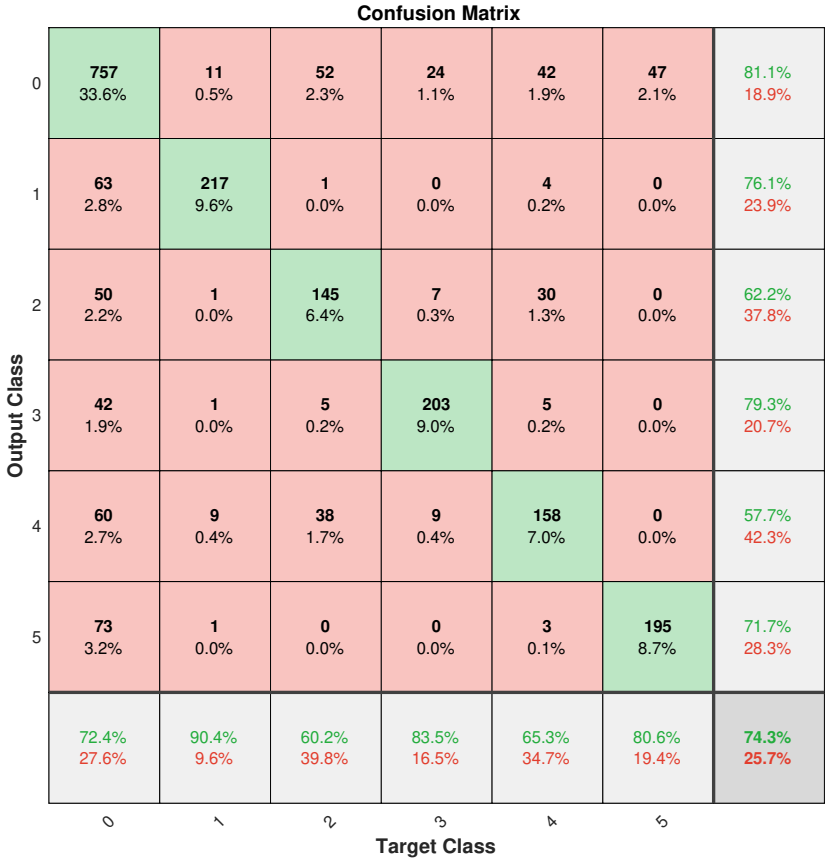

Figure 6.6: CM, 16 Electrodes

Another attempt was to do feature analysis. In feature analysis, the goal would be to make selective combinations of individual electrodes (since each electrode only incorporates one feature, which is amplitude), and check if the combination would reach higher accuracy in the SVM classifier. The program ran for approximately 30 hours and did not stop, so given the high computational expense of this procedure, the results were inconclusive as well. It was also important to point out that the results, particularly of this classifier, were performed by the subject already familiarised with the entire training procedure. The results presented are the best accuracy that was able to be produced, taking into account that the first one had an accuracy for approximately 70%.
In a last effort to try to prove the cross-talk between electrodes, a script was written in order to subtract the signals of consecutive electrodes. In the end, there were 15 signals instead of the 16 previous. The goal of this was to remove a common component present in closely spaced electrodes. A new model was built and a new confusion matrix was obtained. A fully detailed information of the confusion-matrixes can be seen in Appendix C. The results have shown the increase in classification from 72.2% to 77.7% using an LDA classifier and from 74.3% to 78.8% with the SVM classifier. This technique has proved that there is a common component between all the electrodes. This information is ”overfeeding” the classifier and is not adding relevant information.
In support of the hypothesis of cross-talk between electrodes of the high density armband used, it is possible to see that, by using the same number of electrodes but smaller in size, the classification accuracy did not drop as much, which means that in fact there might be an ”overfeed” of information in training the classifier with a larger amount of electrodes. Furthermore, with the decrease of the electrode size, there was not anything that would make it better except an increase in the performance of the classifier as, after all, the SENIAM recommendations do not recommend the use of circular electrodes with less than 10 mm in diameter.

6.3 Conslusion

All in all, the results provided by this chapter have shed some light on how increasing the number of electrodes and changing their size impacts the classification accuracy. Te results have shown partially what would be expected as the classification dropped with the decrease in electrode side. On the other hand the classification dropped unexpectedly with the increase of electrode numbers, showing that 8 electrodes of 10 mm has had a best classification accuracy so far. In the next chapter, studies will be performed regarding the

classification in a multi-subject setup. Furthermore, in order to better assess the industry applications of this classification, a classifier with the EMG provided by 3-different subjects will be built.

Chapter 7

Multi-Subject Tests

7.1 Introduction

One of the inherent factors of the development of this project has to do with the entire training process of the classifier. Since the accuracy results depend directly on this training process, and given that the only results provided so far are performed by the subject who built the entire system, this raises questions regarding the applicability of the developed system in a multi-patient setup.
One of the inherent parts of this project, mentioned earlier in this report, had to do with the MatLab user interface. In order to make the classification of a process easy and intuitive, this needs to be presented to the subject in a way that he can readily understand. The development of this user interface is not a part of this project, but it is easy to understand how the subject's familiarity has with the system influences the overall results of the classification of this process.
In order to solve this issue, that is, to examine the results of the project when tested in more patients, the following process was developed.

7.2 Methodology

Given the results obtained in the previous chapter, the classification accuracy of the setup did not improve neither with the increment of the electrode density nor with the decrease in size of the electrodes, the structure used for the tests in this chapter is the original 8-electrode armband where each electrode had 10 mm in diameter. The methodology for training the classifier was the same as in Chapter 5.6. Time was given to the subjects so they could familiarise themselves with the platform and how the system worked. The process was repeated as many times as necessary, until acceptable values of accuracy were

achieved.

7.3 Results

Table 7.1 presents the classification results of each subject in each trial. As it is possible to see, Subject 1 required 5 trials until it was possible to obtain a classification accuracy of 83%, whilst subject 2 managed to obtain a better accuracy value in two trials. Figures 7.1 and 7.2 present the confusion matrixes for the best results of each subject. As it is possible to see from the results, despite the lower classification accuracy, one of the recurrent problems is the miss-classification of rest. Despite this fact, the overall results of each subjet match the results shown in the previous chapter. There is a nice distribution of the classification across all classes, being that fist flexion (class 3) usually remains the one with the highest true positive rate.

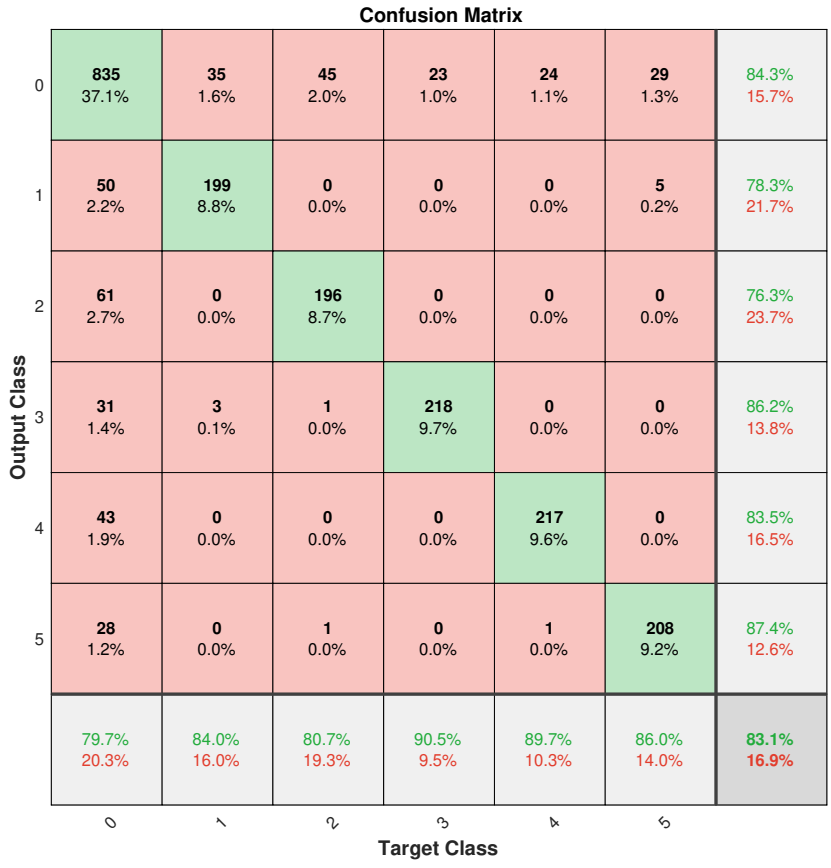

Figure 7.1: CM, SVM Subject 1

Trial	Classifier		Subject 1	Subject 2
1	LDA	3 Class	62.6%	68.1%
		5 Class	57.4%	60.6%
	SVM	3 Class	68.5%	77.3%
		5 Class	70.3%	74.3%
2	LDA	3 Class	69.1%	82.5%
		5 Class	63.4%	80.2%
	SVM	3 Class	83.4%	85.9%
		5 Class	72.6%	87.1%
3	LDA	3 Class	70.0%	-
		5 Class	60.2%	-
	SVM	3 Class	78.0%	-
		5 Class	73.1%	-
4	LDA	3 Class	65.7%	-
		5 Class	59.3%	-
	SVM	3 Class	71.9%	-
		5 Class	70.8%	-
5	LDA	3 Class	78.1%	-
		5 Class	77.5%	-
	SVM	3 Class	81.1%	-
		5 Class	83.1%	-

Table 7.1: Classification Accuracy Results for multi subject with trial number

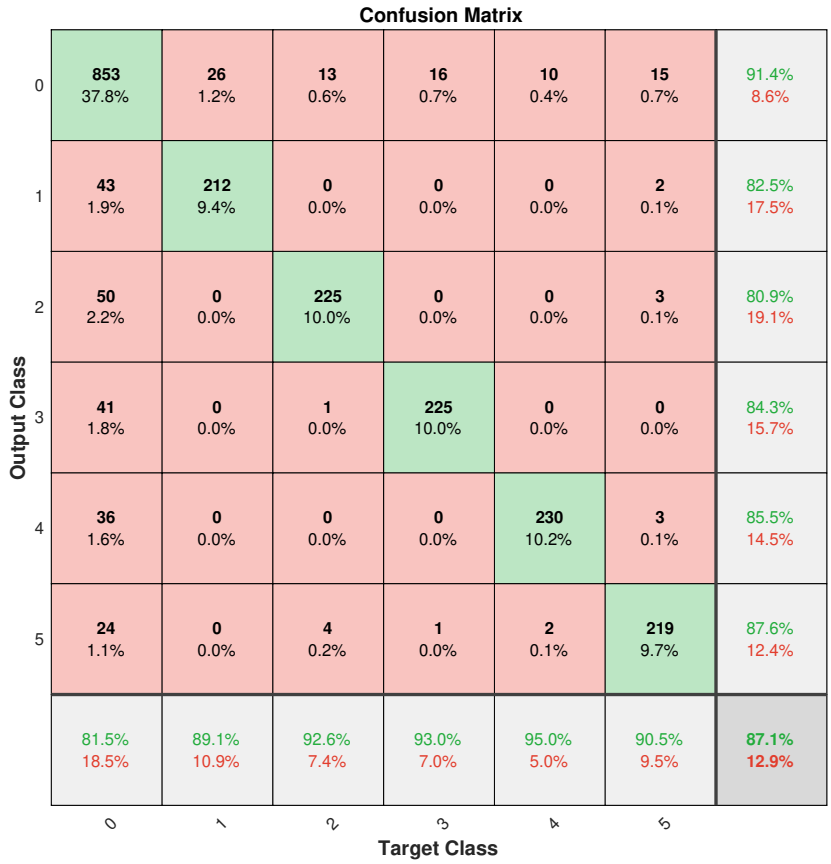

Figure 7.2: CM, SVM Subject 2

7.4 Discussion and Conclusion

In this chapter, two subjects were asked to perform the training procedure using the Pi-ETPU armband. As it was expected, in the initial trainings, the accuracy values are low due to the unfamiliarity of the user with the training process. This factor proves just how dependent the accuracy results are on the user's familiarity with the system. Overall, subject 1 took five trials to obtain an accuracy of approximately 80%, while subject 2 took only two trials. When the subjects were asked about the training process, the common response was that the interface was fairly intuitive, although the images displayed lacked in quality. This would then raise doubts on which movement should be performed.

Furthermore, the miss-classification of rest comes from the training procedure. during the training process, this is a section where the user should remain at rest and then start contracting slowly. One common problem noticed by the users is that they would start the contraction before the right time. All the data from the recording is used, that is, although previous rest recording was performed in each movement contraction, the flat line of the plot is also used to determine rest. If the user does not perform this correctly, then there will be

a miss-classification of rest, as the results have shown.

All in all, this chapter serves to prove how the technique used to classify movements using Pi-ETPU-based electrodes works in a multi-subject environment.

Chapter 8

The Future

8.1 The Author's Perspective

This project has shown the capability of a fairly simple system used in classifying discrete movements, via the use of EMG signals, acquired via 3D printed Pi-ETPU electrodes. In this chapter, several points about the entire system will be covered regarding improvements that will help in the future development of this project.

8.2 Armband Design

The project covers the development of the electrodes with a fairly primitive design. As it is not practical for an upper limb assistive device to be working with a set of cables attached to them, the overall design of the armband is one of the first reformulations that has to be done.

First, the goal of 3D printing in this project is to easily produce a system that is adaptable to the user. In this case, the printing bed is too small, which means that it is not possible to create a single structure which could cover the entire perimeter of the lower arm. This is a limitation of the setup itself, which was overcome by simply printing the structure in two parts. This generated a couple of problems, the first of which being that, in order to save time, each subject used the same structure. Since not every subject had similar arm perimeters, the electrodes were not perfectly aligned and the armband was not tight enough to the arm. These are two major conditions for good results in this project. A good connection and a correct alignment of the electrodes are essential.

Second, the connection of the electrodes needs to be improved as well. In a real life situation, it is not feasible to have 8 electrodes with connected cables. My suggestion in the

first stage of developments would be to maintain the 8-electrode armband composed of 10 mm diameter electrodes, and build a system for wireless transmission of EMG information. It would be fair to assume a direct conversion of frequency to bit/s since the entire classification process only looks at the amplitude of EMG. Then, the current system would sample at 1250 Hz which would mean a flow of 2Kb/s of information. This is far below the limitations of current wireless transmission systems such as bluetooth. On the other hand, this would also entail that the signal processing of the system needs to be improved.
Last but not least, in a not so far distant future, the full process of classification would also be done online. crgkThe larger level of accuracy of SVM in comparison to LDA was discussed in this report. This can be particularly assessed when, by incrementing the number of classes, classification accuracy drops faster in LDA while SVM the drop is more mild. On the other hand, SVM requires a higher level of computational effort. Microprocessors such as intel i7 can be made to work in a wireless system since they have a very small size and high computational capabilities. On the other hand, this raises questions regarding the cost-balance of the final device, as well as, the power consumption of the device, which are also a great limitation for prosthetic devices. There is a wide variety of processors in the market and an in-depth study regarding the advantages and disadvantages of each and one of them should be performed. For example, RISC processors (i.e. ARM-X based chips), can use much less power than its counterparts.
Ultimately, given the nature of the printing procedure, it would be extremely interesting to develop, for each user, a size-specific bracelet with electrodes that would tightly fit into a robotic arm-socket. That way the electrodes would never have to be removed, eliminating the problems that the majority of literature reports, that is, constantly having to train a classifier due to the movement of the electrodes.

8.3 Classification Improvement

It was repeated many times in this report how the classifications only allowed for the distinction between discreet movements. This limitation comes from the classifier itself and not from the setup. SVM, LDA, and Neural Networks are systems that only allow for the discrimination between classes. On the other hand, linear regression (another type of classification learner) uses muscle activation in order to predict positions on a 2D plate. If it would be possible to make a hybrid classifier, then it would be possible to build a classifier that would not only allow to distinguish between movements, but to determine the position of the prosthesis.

8.4 Overall Conclusion

This project has allowed, in the time-span available, to make a partial model of charge transfer inside a circular Pi-ETPU electrode. Furthermore, the signal acquired with these electrodes has proved to be equal to, or better than, the classification of discrete movements using the state of the art technologies for prosthetics control, when compared to the current state of the art electrodes.

Last but not least, this project opens the door for more development into 3D-printed electrodes and their incorporation into currently made devices. Given the basis of the infrastructure, this last chapter has covered 3 mains points through which the investigation can move on.

Bibliography

[1] Comprehensive, “Upper Extremety Prosthesis,” 2018.

[2] T. Bionics, “I-Limb.”

[3] O. van der Niet, H. A. Reinders, H. Bouwsema, R. M. Bongers, and C. K. van der Sluis, “the I-Limb Pulse Hand Compared To the I-Limb and Dmc Plus Hand,” pp. 0–1, 2011.

[4] Cnet, “Touch Bionics i-limb prosthesis is controlled by an iPhone app.”

[5] D. Sadhankar and A. Sasankar, “An overview and comparison of Software Reliability tools,” *IOSR Journal of Computer Engineering*, pp. 2278–661.

[6] D. Cotton, A. Cranny, P. Chappell, N. White, and S. Beeby, “Control strategies for a multiple degree of freedom prosthetic hand,” *UKACC Control 2006 Mini Symposia*, vol. 2006, pp. 211–218, 2006.

[7] P. J. Kyberd, O. E. Holland, P. H. Chappell, S. Smith, R. Tregidgo, P. J. Bagwell, and M. Snaith, “MARCUS: A Two Degree of Freedom Hand Prosthesis with Hierarchical Grip Control,” *IEEE Transactions on Rehabilitation Engineering*, vol. 3, no. 1, pp. 70–76, 1995.

[8] R. N. Khushaba, S. Kodagoda, M. Takruri, and G. Dissanayake, “Toward improved control of prosthetic fingers using surface electromyogram (EMG) signals,” *Expert Systems with Applications*, vol. 39, no. 12, pp. 10731–10738, 2012.

[9] K. Englehart and B. Hudgins, “A robust, real-time control scheme for multifunction myoelectric control,” *Biomedical Engineering, IEEE Transactions on*, vol. 50, no. 7, pp. 848–854, 2003.

[10] J. Yousefi and A. Hamilton-Wright, “Characterizing EMG data using machine-learning tools,” *Computers in Biology and Medicine*, vol. 51, pp. 1–13, 2014.

[11] W. P. Warren S. McCulloch, “A Logical Calculus of the Ideas Immanent in Nervous Activity,” vol. 5, pp. 115–133, 1943.

[12] C.Cortes and V.Vapnik, “Support Vector Networks,” *Machine Learning*, vol. 20, no. 3, pp. 273˜–˜297, 1995.

[13] H. Packard, “HP 4284a Precision LCR- Meter Operation Manual,” no. Sixth, 1998.

[14] H. J. Hermens, B. Freriks, R. Merletti, D. Stegeman, J. Blok, G. Rau, C. Disselhorst-Klug, and G. Hägg, “European Recommendations for Surface ElectroMyoGraphy,” *Roessingh Research and Development*, pp. 8–11, 1999.

[15] J. G. Webster, “Medical instrumentation: Application and design,” *Control Engineering Practice*, vol. 5, no. 2, pp. 295–296, 1997.

[16] J. Niu, B. E. Conway, and W. G. Pell, “Comparative studies of self-discharge by potential decay and float-current measurements at C double-layer capacitor and battery electrodes,” *Journal of Power Sources*, vol. 135, no. 1-2, pp. 332–343, 2004.

[17] S. R. Taylor and E. Gileadi, “Physical interpretation of the Warburg impedance,” *Corrosion*, vol. 51, no. 9, pp. 664–671, 1995.

[18] M. B. Reaz, M. S. Hussain, and F. Mohd-Yasin, “Techniques of EMG signal analysis: Detection, processing, classification and applications,” *Biological Procedures Online*, vol. 8, no. 1, pp. 11–35, 2006.

[19] TMSi+, “Refa,” in *Refa User Manual*, pp. 1–23, 2017.

[20] . Merletti, R.1; Rainoldi, A.1,2; Farina, D.1, “Surface Electromyography for Noninvasive Characterization of... : Exercise and Sport Sciences Reviews,” no. c, 2001.

[21] S. Journal, “Danish National Research Centre for the Working Environment Norwegian National Institute of Occupational Health Finnish Institute of Occupational Health,” 2015.

[22] C. J. D. Luca, “Surface Electromyography : D Etection and R Ecording,” *DelSys Incorporated*, vol. 10, no. 2, pp. 1–10, 2002.

[23] C. J. De Luca, L. Donald Gilmore, M. Kuznetsov, and S. H. Roy, “Filtering the surface EMG signal: Movement artifact and baseline noise contamination,” *Journal of Biomechanics*, vol. 43, no. 8, pp. 1573–1579, 2010.

[24] D. Farina and R. Merletti, “Comparison of algorithms for estimation of EMG variables during voluntary isometric contractions,” *Journal of Electromyography and Kinesiology*, vol. 10, no. 5, pp. 337–349, 2000.

[25] A. J. Young, L. H. Smith, E. J. Rouse, and L. J. Hargrove, "Surface EMG Pattern Recognition," *1250 Ieee Transactions on Biomedical Engineering,*, vol. 60, no. 5, pp. 1250–1258, 2013.

[26] P. Geethanjali, "Myoelectric control of prosthetic hands: state-of-the- art review," *Medical Devices: Evidence and Research*, vol. 9, pp. 247–255, 2016.

[27] E. Union, "SoftPro Project."

[28] C. M. Bishop, *Pattern Recognition and Machine Learning*, vol. 53. 2013.

[29] A. Tharwat, T. Gaber, A. Ibrahim, and A. E. Hassanien, "Linear discriminant analysis: A detailed tutorial," *AI Communications*, vol. 30, no. 2, pp. 169–190, 2017.

[30] M. F. Lucas, A. Gaufriau, S. Pascual, C. Doncarli, and D. Farina, "Multi-channel surface EMG classification using support vector machines and signal-based wavelet optimization," *Biomedical Signal Processing and Control*, vol. 3, no. 2, pp. 169–174, 2008.

[31] A. Subasi, "Classification of EMG signals using PSO optimized SVM for diagnosis of neuromuscular disorders," *Computers in Biology and Medicine*, vol. 43, no. 5, pp. 576–586, 2013.

[32] R. a. Mezzarane, L. a. Elias, F. H. Magalhaes, V. M. Chaud, and a. F. Kohn, "Experimental and simulated EMG responses in the study of the human spinal cord," *Electrodiagnosis in new frontiers of clinical research*, no. May 2014, pp. 57–87, 2013.

[33] R. Merletti, A. Holobar, and D. Farina, "Analysis of motor units with high-density surface electromyography," *Journal of Electromyography and Kinesiology*, vol. 18, no. 6, pp. 879–890, 2008.

[34] H. Daley, K. Englehart, L. Hargrove, and U. Kuruganti, "High density electromyography data of normally limbed and transradial amputee subjects for multifunction prosthetic control," *Journal of Electromyography and Kinesiology*, vol. 22, no. 3, pp. 478–484, 2012.

[35] L. Pan, D. Zhang, N. Jiang, X. Sheng, and X. Zhu, "Improving robustness against electrode shift of high density EMG for myoelectric control through common spatial patterns," *Journal of NeuroEngineering and Rehabilitation*, vol. 12, no. 1, pp. 1–16, 2015.

Appendix A

Support Vector Machine (SVM)

A.1 Simplification of the width expression

Given equation A.1, a constrain that establishes the samples that lie in the edges of the street, and Equation A.2 that establishes the width of the street.

$$y_i(\vec{x}_i \cdot \vec{\omega} + b) - 1 \geq 0 \tag{A.1}$$

$$Width = (\vec{x}_+ - \vec{x}_-) \cdot \frac{\vec{\omega}}{||\vec{\omega}||} \tag{A.2}$$

$$\begin{aligned} y_i(\vec{x}_+ \cdot \vec{\omega} + b) - 1 = 0 \\ y_i(\vec{x}_- \cdot \vec{\omega} + b) - 1 = 0 \end{aligned} \tag{A.3}$$

Furthermore, Equation , establishes the maximum width, which in turn is determined by the samples that lie in edged in the street. So for positive samples its possible to obtain, the following expression, taking into account that if it's a positive sample, $y_i = 1$.

$$\begin{aligned} y_i(\vec{x}_+ \cdot \vec{\omega} + b) - 1 = 0 \\ \vec{x}_+ \cdot \vec{\omega} + b - 1 = 0 \\ \vec{x}_+ \cdot \vec{\omega} = 1 - b \end{aligned} \tag{A.4}$$

But also for a negative sample, remembering that for any negative sample, it has been

established $y_i = -1$.

$$\begin{aligned} y_i(\vec{x}_- \cdot \vec{\omega} + b) - 1 &= 0 \\ -(\vec{x}_- \cdot \vec{\omega} + b) - 1 &= 0 \\ -(\vec{x}_- \cdot \vec{\omega} + b) &= 1 \\ \vec{x}_- \cdot \vec{\omega} + b &= -1 \\ \vec{x}_- \cdot \vec{\omega} &= -1 - b \end{aligned} \tag{A.5}$$

Inputting Equations A.4 and A.5 in Equation A.2, it is possible to obtain the simplified version of the width of the street, as presented in Chapter 5.5.2.

$$\begin{aligned} Width &= (\vec{x}_+ - \vec{x}_-) \cdot \frac{\vec{\omega}}{||\vec{\omega}||} \\ Width &= [(\vec{x}_+ \cdot \vec{\omega}) - (\vec{x}_- \cdot \vec{\omega})] \frac{1}{||\omega||} \\ Width &= [(1 - b) - (-1 - b)] \frac{1}{||\omega||} \\ Width &= [1 - b + 1 + b] \frac{1}{||\omega||} \\ Width &= \frac{2}{||\omega||} \end{aligned} \tag{A.6}$$

A.2 Lagrange Derivatives

The original Lagrange function, obtained in Chapter 5.5.2 is given by equation A.7.

$$\begin{aligned} L &= \frac{1}{2}||\vec{\omega}||^2 - \sum_{i=1}^{N} \alpha_i [y_i(\vec{\omega} \cdot \vec{x}_i + b) - 1] \\ L &= \frac{1}{2}||\vec{\omega}||^2 - \sum_{i=1}^{N} \alpha_i y_i \vec{\omega} \cdot \vec{x}_i - \sum_{i=1}^{N} \alpha_i y_i b + \sum_{i=1}^{n} \alpha_i 1 \end{aligned} \tag{A.7}$$

The partial derivative of L in respect to $\vec{\omega}$ is presented in Equation A.8, and the partial derivative of L in regards to b is presented in Equation A.9. It is proved that the differentiation of vectors is similar, mathematically similarly as the differentiation of scalars. That can be proved by the differentiation of the vector by expanding it in term of all the vector

components.

$$\begin{aligned}
\frac{\partial L}{\partial \vec{\omega}} &= \frac{\partial}{\partial \vec{\omega}}[\frac{1}{2}||\vec{\omega}||^2] - \frac{\partial}{\partial \vec{\omega}}[\sum_{i=1}^{N} \alpha_i y_i \vec{\omega} \cdot \vec{x}_i] - \frac{\partial}{\partial \vec{\omega}}[\sum_{i=1}^{N} \alpha_i y_i b] + \frac{\partial}{\partial \vec{\omega}}[\sum_{i=1}^{n} \alpha_i 1] \\
\frac{\partial L}{\partial \vec{\omega}} &= \vec{\omega} - \sum_{i=1}^{N} \alpha_i y_i \vec{x}_i - 0 + 0 \\
\frac{\partial L}{\partial \vec{\omega}} &= \vec{\omega} - \sum_{i=1}^{N} \alpha_i y_i \vec{x}_i \implies \vec{\omega} = \sum_{i=1}^{N} \alpha_i y_i \vec{x}_i
\end{aligned} \tag{A.8}$$

$$\begin{aligned}
\frac{\partial L}{\partial b} &= \frac{\partial}{\partial b}[\frac{1}{2}||\vec{\omega}||^2] - \frac{\partial}{\partial b}[\sum_{i=1}^{N} \alpha_i y_i \vec{\omega} \cdot \vec{x}_i] - \frac{\partial L}{\partial b}[\sum_{i=1}^{N} \alpha_i y_i b] + \frac{\partial}{\partial b}[\sum_{i=1}^{n} \alpha_i 1] \\
\frac{\partial L}{\partial b} &= 0 - 0 - \sum_{i=1}^{N} \alpha_i y_i + 0 \\
\frac{\partial L}{\partial b} &= \sum_{i=1}^{N} \alpha_i y_i \implies \sum_{i=1}^{N} \alpha_i y_i = 0
\end{aligned} \tag{A.9}$$

In order to find the maximum and minimum of the equation, the derivatives must be placed to zero from which the conditions that arise are the same as presented in Chapter 5.5.2. Plugging Equation A.8 into A.7 gives equation A.10.

$$\begin{aligned}
L &= \frac{1}{2}(\sum_{i=1}^{N} \alpha_i y_i \vec{x}_i) \cdot (\sum_{j=1}^{N} \alpha_j y_j \vec{x}_j) - (\sum_{i=1}^{N} \alpha_i y_i \vec{x}_i) \cdot (\sum_{j=1}^{N} \alpha_j y_j \vec{x}_j) - b \sum_{i=1}^{n} \alpha_i y_i + \sum_{i=1}^{N} \alpha_i \\
L &= \sum_{i=1}^{N} \alpha_i + \frac{1}{2} \sum_{i=1}^{N} \sum_{j=1}^{N} \alpha_i \alpha_j y_i y_j \vec{x}_i \cdot vecx_j - \sum_{i=1}^{N} \sum_{j=1}^{N} \alpha_i \alpha_j y_i y_j \vec{x}_i \cdot vecx_j - b \sum_{i=1}^{n} \alpha_i y_i
\end{aligned} \tag{A.10}$$

And from Equation A.9 we get Equation A.11 as in section 5.5.2.

$$\begin{aligned}
L &= \sum_{i=1}^{N} \alpha_i + \frac{1}{2} \sum_{i=1}^{N} \sum_{j=1}^{N} \alpha_i \alpha_j y_i y_j \vec{x}_i \cdot \vec{x}_j - \sum_{i=1}^{N} \sum_{j=1}^{N} \alpha_i \alpha_j y_i y_j \vec{x}_i \cdot vecx_j - 0 \\
L &= \sum_{i=1}^{N} \alpha_i - \frac{1}{2} \sum_{i=1}^{N} \sum_{j=1}^{N} \alpha_i \alpha_j y_i y_j \vec{x}_i \cdot \vec{x}_j
\end{aligned} \tag{A.11}$$

Appendix B

Electrode Functionality Analysis

B.1 Classification Results

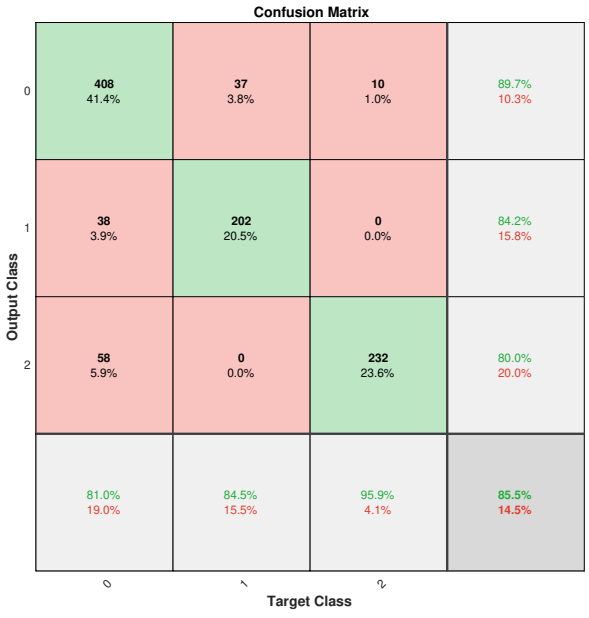

Figure B.1: LDA 3-Class AgCl

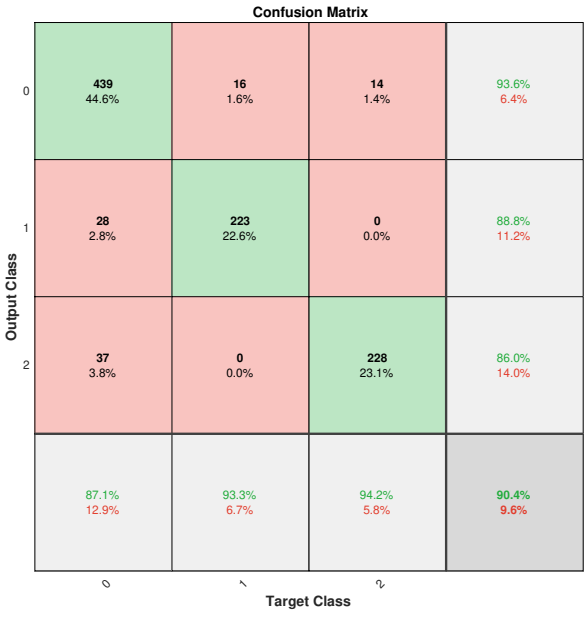

Figure B.2: SVM 3-Class AgCl

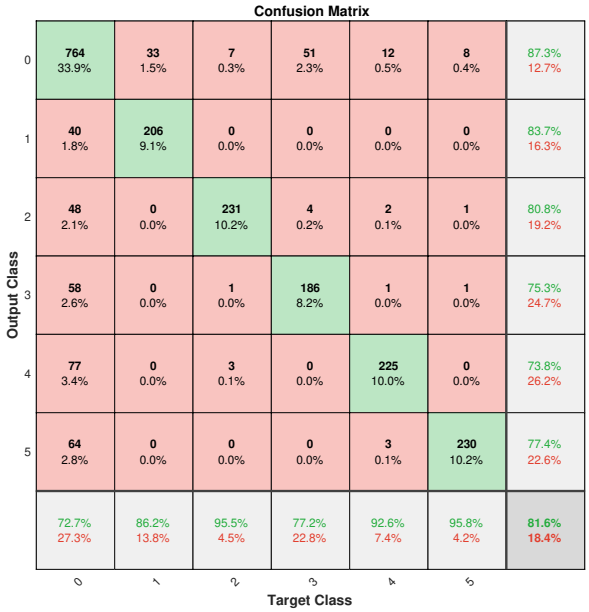

Figure B.3: LDA 5-Class AgCl

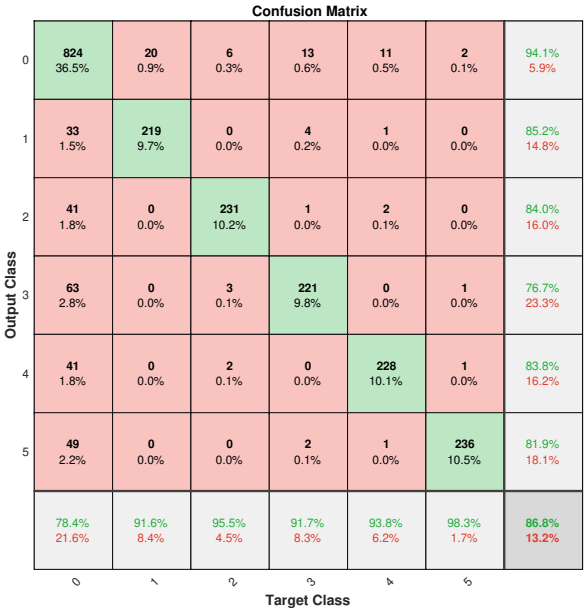

Figure B.4: SVM 5-Class AgCl

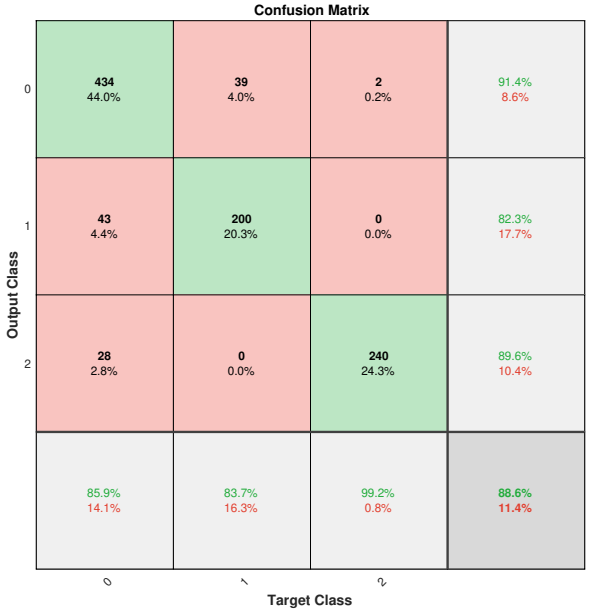

Figure B.5: LDA 3-Class Pi-ETPU

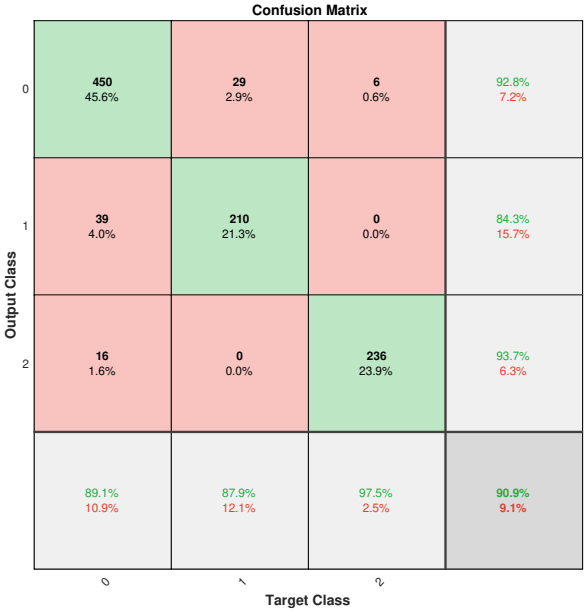

Figure B.6: SVM 3-Class Pi-ETPU

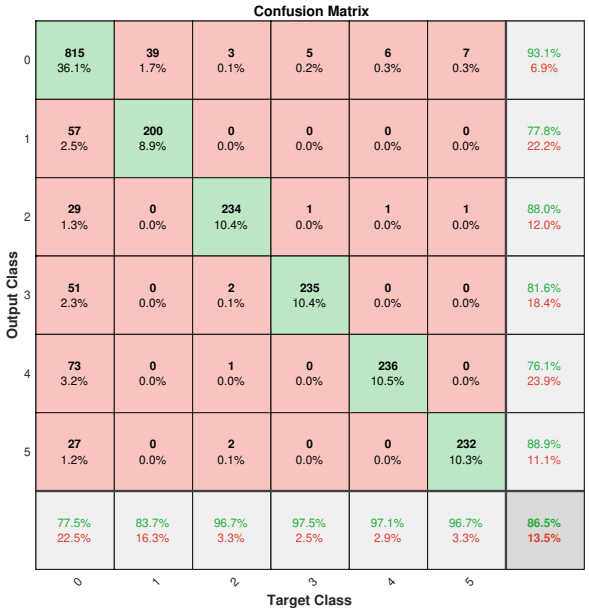

Figure B.7: LDA 5-Class Pi-ETPU

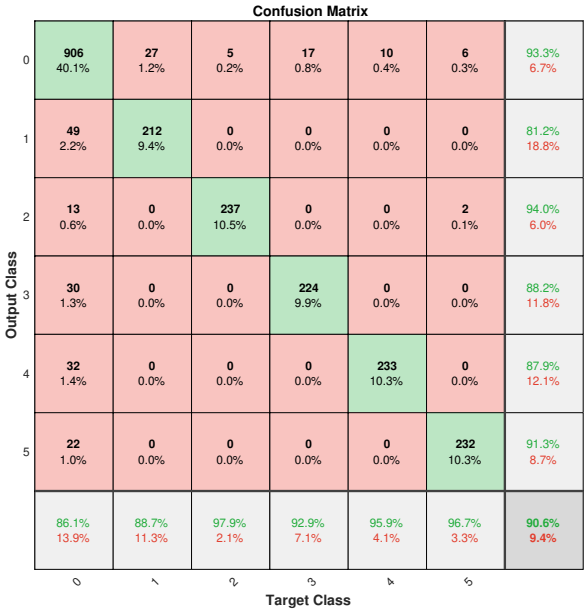

Figure B.8: SVM 5-Class Pi-ETPU

Appendix C

16 Electrodes Common Component Analysis

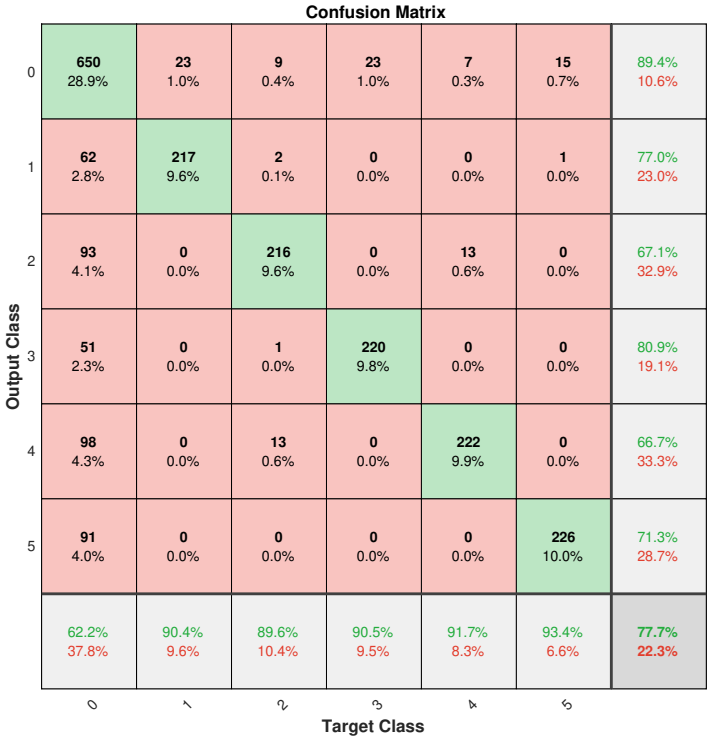

Figure C.1: CM, LDA without common component

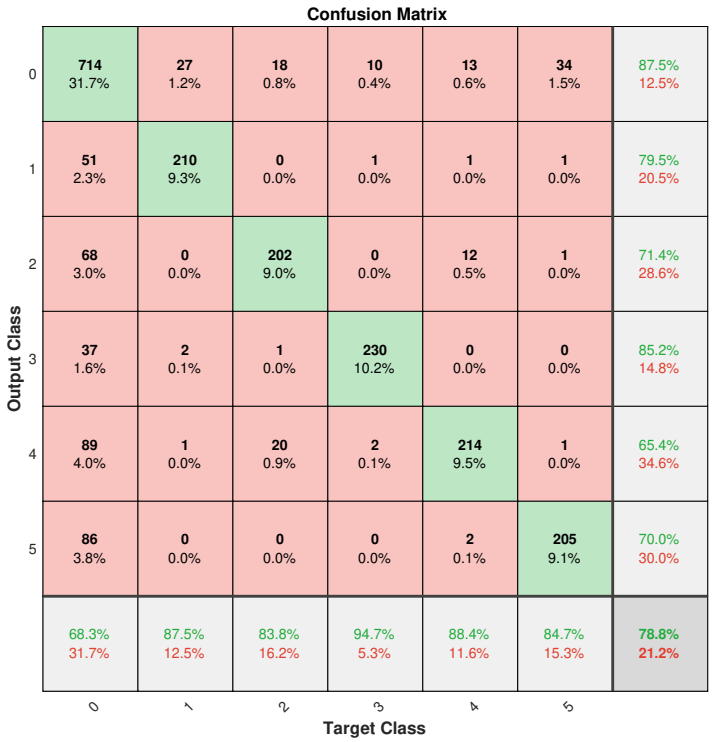

Figure C.2: CM, SVM without common component

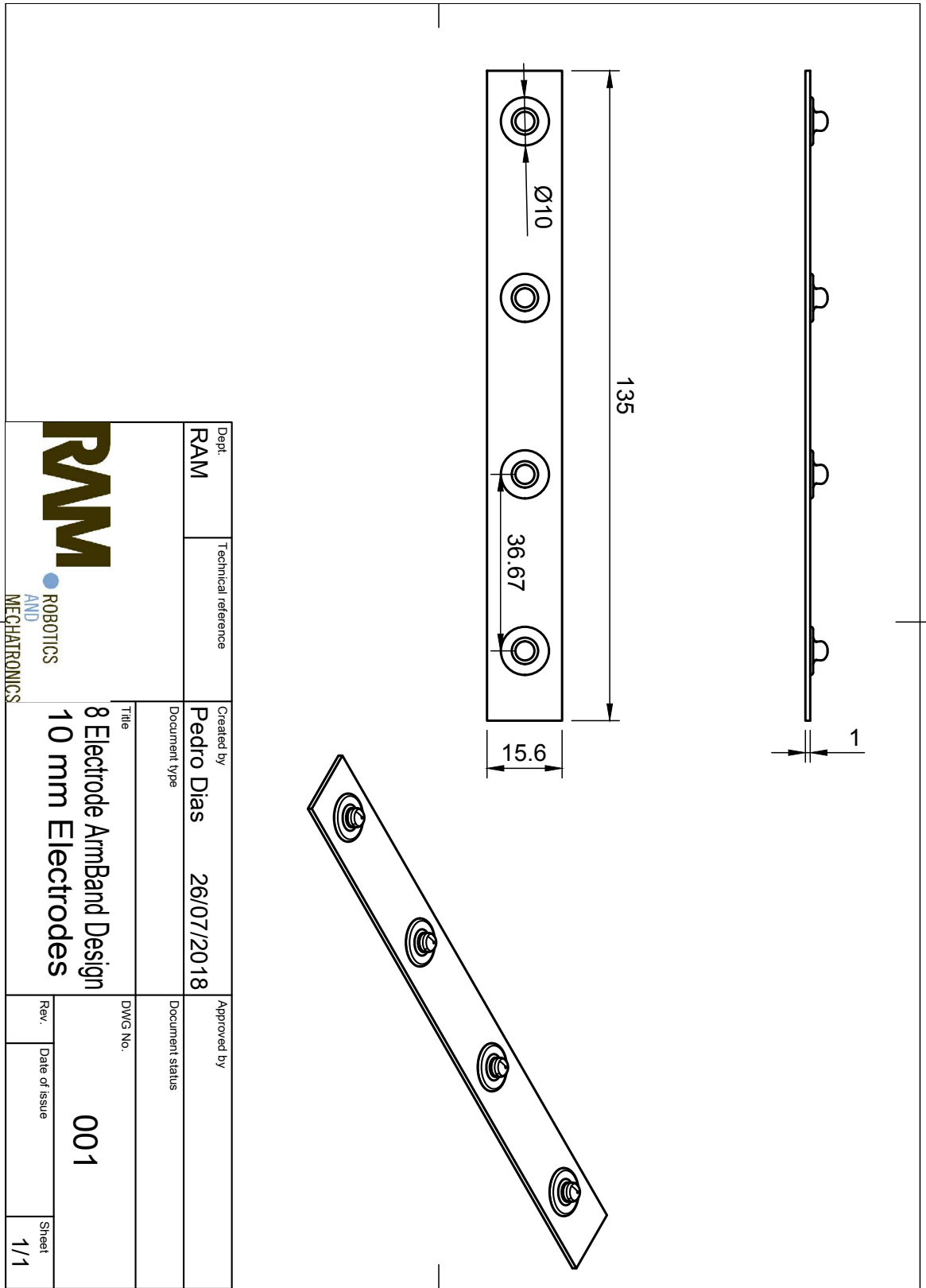

Dept. RAM	Technical reference	Created by Pedro Dias	26/07/2018
		Document type	Approved by
Title 8 Electrode ArmBand Design 10 mm Electrodes			Document status
		DWG No. 001	
	Rev.	Date of issue	Sheet 1/1

RAM ROBOTICS AND MECHATRONICS

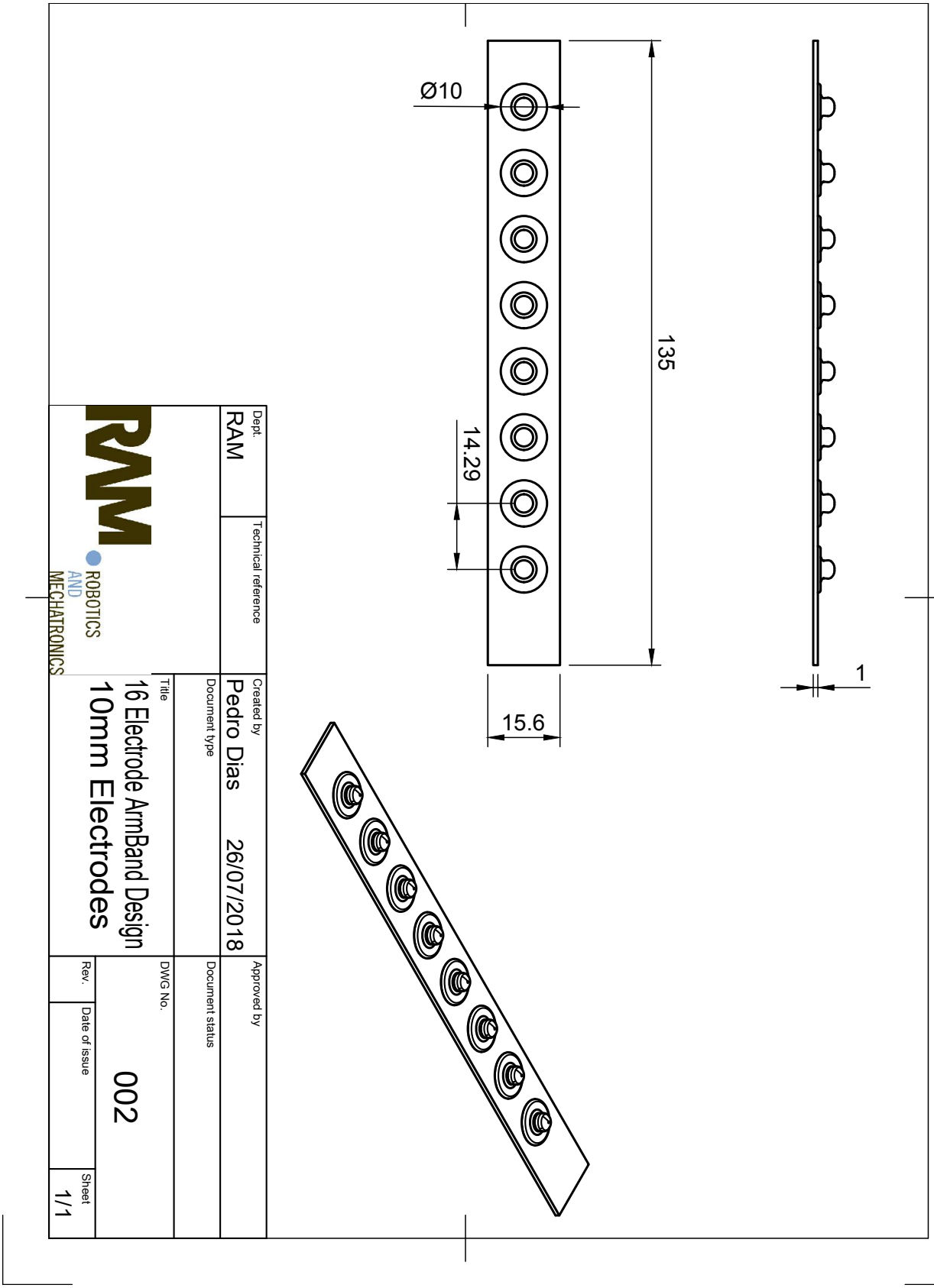
Ø10
135
14.29
15.6
1
RAM
ROBOTICS AND MECHATRONICS
Dept.
RAM
Technical reference
Created by
Pedro Dias
26/07/2018
Document type
Approved by
Document status
Title
16 Electrode ArmBand Design
10mm Electrodes
DWG No.
002
Rev.
Date of issue
Sheet
1/1

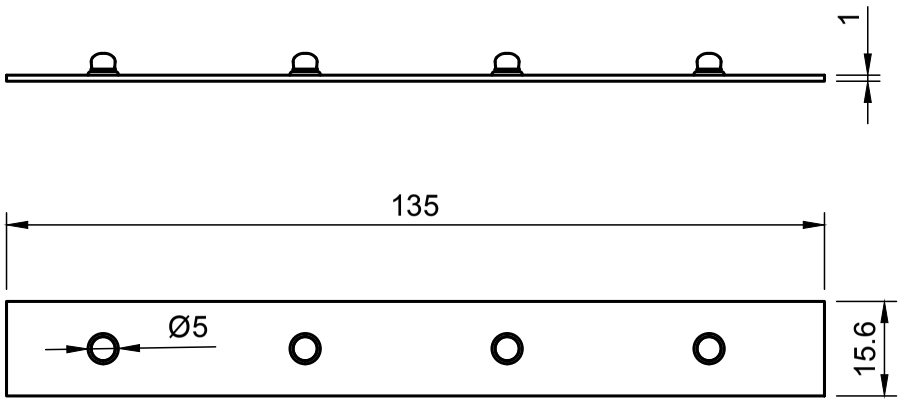

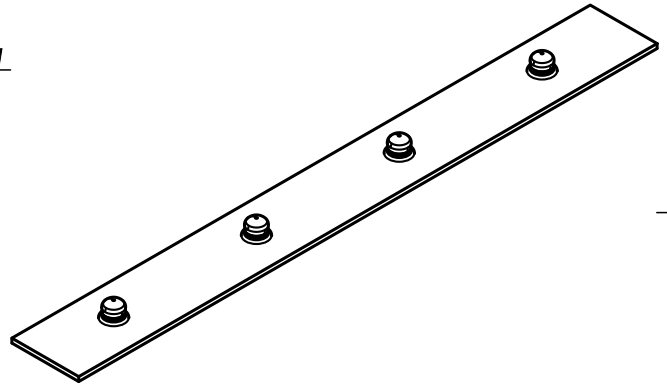

Dept.	Technical reference	Created by	Approved by
RAM		Pedro Dias 26/07/2018	
		Document type	Document status
		Title: 8 Electrode ArmBand Design 5mm Electrodes	DWG No.: 003
			Rev. / Date of issue / Sheet: 1/1

RAM ROBOTICS AND MECHATRONICS